"The Magnetized Interstellar Medium"
8–12 September 2003, Antalya, Turkey
Eds.: B. Uyaniker, W. Reich & R. Wielebinski

Observations of Magnetic Fields in Molecular Clouds

Richard M. Crutcher

Department of Astronomy, University of Illinois, 1002 W. Green St., Urbana, IL 61801

Abstract. Observations of magnetic fields in molecular clouds are essential for understanding their role in the evolution of dense clouds and in the star formation process. The predictions of two extreme paradigms for what drives star formation – magnetic and thermal support with ambipolar diffusion, and compressible turbulence with negligible magnetic fields – are first discussed in order to formulate three tests of the two models that can be applied using observations of magnetic field strengths and morphologies. Techniques for measuring magnetic fields in molecular clouds are described. Three examples of the observational results are discussed here – the low-mass starless core L 183, the young stellar system and molecular outflow NGC 1333 IRAS4A, and the high-mass star formation region DR 21 (OH). Finally, these and all other results of observations of magnetic fields in molecular clouds are used to apply the three tests. The conclusion is that the magnetic support model is consistent with the data, but *both* turbulence and strong magnetic fields are important in the physics of molecular clouds and in the star formation process.

1 Introduction

Observations of magnetic fields in molecular clouds have now become a fairly routine procedure, and many new observational results have been obtained in the last few years. Most progress has been made in mapping polarized emission from dust, but many new Zeeman observations have also been made, together with the first detections of linearly polarized spectral lines. In this article I will both review the observational data and focus on one of the main reasons for observing magnetic fields in molecular clouds – to try to understand their role in the evolution of dense clouds and in the star formation process. Understanding star formation is one of the outstanding challenges of modern astrophysics. However, in spite of significant progress in recent years, there remain unanswered fundamental questions about the basic physics of star formation. In particular, what drives the star formation process? The prevailing view has been that self-gravitating clouds are supported against collapse by magnetic fields, with ambipolar diffusion reducing support in cores and hence driving star formation (e.g., Mouschovias and Ciolek 1999). The other extreme is that molecular clouds are intermittent phenomena in an interstellar medium dominated by turbulence, and the problem of cloud support for long time periods is irrelevant (e.g., Elmegreen 2000). In this paradigm, clouds form and disperse by the operation of compressible turbulence, with clumps sometimes becoming gravitationally bound. Turbulence then dissipates rapidly, and the cores collapse to form stars. Hence, there are two competing models for driving the star formation process. The fundamental issue of what drives star formation is far from settled, on either observational or theoretical grounds. In this contribution I focus on discussing how observations of magnetic fields in molecular clouds can distinguish between and test these models.

2 Model Predictions and Observational Tests

The ambipolar diffusion and turbulence models for driving star formation have different predictions for magnetic field morphology and strength, which form the basis for tests of the two models using observations of magnetic fields. The three main tests of the two models based on observations of magnetic fields involve: (1) the morphology of $\mathbf{B}$, (2) the scaling of $|\mathbf{B}|$ with density and internal velocity dispersion, and (3) the mass to magnetic flux ratio, M/Φ. Of course, it is clear that there are both magnetic fields and turbulence in real clouds. In order to sharpen the distinctions between the two models, here we will consider only the extreme cases of turbulence models with negligibly weak magnetic fields and magnetic support/ambipolar diffusion models without turbulence.

2.1 Morphology

In the magnetic support model, the dominant **B** means field lines should be smooth, without irregular structure. Clouds will be thin disks or oblate spheroids, since thermal pressure provides the only support along field lines. The field lines should be parallel to the minor axes of clouds. Finally, an original morphology with parallel magnetic field lines will be transformed into an hourglass morphology since it is the tension of the bent field lines that provides support. In the turbulent model, **B** will be too weak to resist twisting by the dominant turbulence, and field lines will not be smooth but chaotic, with small-scale irregular structure. No correlation with cloud morphology is expected.

2.2 Scaling

The scaling of $|\mathbf{B}|$ with density ρ is usually parameterized as $|\mathbf{B}| \propto \rho^{\kappa}$, so our discussion will be in terms of κ. Since the ambipolar diffusion timescale is much shorter in a core than in an envelope, the core will become supercritical and collapse while the envelope remains subcritical and supported by the field. Hence, $|\mathbf{B}|$ in cloud envelopes remains virtually unchanged, so at lower densities no strong correlation between $|\mathbf{B}|$ and density ρ is predicted, and $\kappa \sim 0$. As ambipolar diffusion increases M/Φ in a core, ρ increases faster than $|\mathbf{B}|$ and $\kappa > 0$. After the core becomes supercritical, it will collapse much more rapidly than the ambipolar diffusion rate; the collapse approaches proceeding with flux freezing, so κ will increase and approach a limit of 0.5. In turbulent models, in the low-density case before gravity becomes important no relation is expected between the magnetic field strength and other parameters such as density; so again, on average, $\kappa \sim 0$. Once gravity becomes important, a rough equipartition of energies is achieved. If we assume virial equilibrium between gravity and turbulence ($3GM^2/5R = 3M\sigma^2/2$), then $\rho R^2 \propto \sigma^2$. Flux freezing ($M \propto \Phi$) gives $\rho R \propto |\mathbf{B}|$, so $|\mathbf{B}| \propto \sigma\rho^{1/2}$ is predicted. Hence, although both models predict $\kappa \approx 0.5$ for collapsing cores, if turbulence provides significant support an additional scaling of $|\mathbf{B}|$ with the turbulent velocity dispersion σ is predicted.

2.3 Mass-to-flux ratio

The ratio of the mass in a magnetic flux tube to the magnitude of the magnetic flux is a crucial parameter for the magnetic support/ambipolar diffusion model. If we assume virial equilibrium between gravity and the magnetic field, $3GM^2/5R = B^2R^3/3$ (for a uniform sphere), then the critical mass to flux ratio $(M/\Phi)_{\rm crit}$ may be found by solving for $(M/\Phi)_{\rm crit} \equiv M/\pi R^2 B = [3\pi\sqrt{G/5}]^{-1}$. However, since magnetically supported clouds will be thin disks, the more relevant $(M/\Phi)_{\rm crit}$ is that for a uniform disk, which is $(M/\Phi)_{\rm crit} = [2\pi\sqrt{G}]^{-1}$ (Nakano and Nakamura 1978); the precise value of the numerical coefficient is slightly model (geometry) dependant. It is convenient to state M/Φ in units of the critical value, and to define $\lambda \equiv (M/\Phi)_{\rm actual}/(M/\Phi)_{\rm crit}$. Inferring λ from observations is possible if the column density N and the magnetic field strength $|\mathbf{B}|$ are measured:

$$\lambda = \frac{(M/\Phi)_{\rm observed}}{(M/\Phi)_{\rm crit}} = \frac{mNA/|\mathbf{B}|A}{1/2\pi\sqrt{G}} = 7.6 \times 10^{-21} \frac{N(H_2)}{|\mathbf{B}|} \qquad (1)$$

where $m = 2.8m_{\rm H}$ allowing for He, A is the cloud area of the observations, $N(H_2)$ is in cm^{-2}, and $|\mathbf{B}|$ is in μG. In the ambipolar diffusion model clouds are initially subcritical, $\lambda < 1$. Ambipolar diffusion is fastest in shielded, high-density cores, so cores become supercritical, and rapid collapse ensues. The envelope continues to be supported by the magnetic field. Hence, the prediction is that λ must be < 1 in cloud envelopes, while in collapsing cores λ becomes slightly > 1. Hence, this model tightly constrains λ. On the other hand, the turbulent model imposes no direct constraints on λ, although strong magnetic fields would resist the formation of gravitationally bound clouds by compressible turbulence. Also, if magnetic support is to be insufficient to prevent collapse of self-gravitating clumps that are formed by compressible turbulence, the field must be supercritical, $\lambda > 1$. λ may take any value > 1, although of course for the turbulence model with very weak magnetic fields that we are considering, clouds will be highly supercritical, $\lambda >> 1$.

3 Observational Techniques

3.1 Zeeman splitting

The Zeeman effect is the standard technique for measuring directly magnetic field strengths in molecular clouds (e.g., Crutcher 1993). If a spectral line forming region is permeated by a field **B**, the radiation is split by the normal Zeeman effect into three separate frequencies, $\nu_{\sigma-} = \nu_0 - \nu_Z$, $\nu_\pi = \nu_0$, and $\nu_{\sigma+} = \nu_0 + \nu_Z$, where ν_0 is the line frequency, $\nu_Z = |\mathbf{B}| \times Z$, and Z is the Zeeman sensitivity in Hz/μG. For the 21-cm H I line $Z = 1.4$ Hz/μG, while for molecules with unpaired electrons $Z \sim Z_{\rm H\,I}$. Molecules without an unpaired electron have $Z << Z_{\rm H\,I}$ and (except for the very strong H_2O masers) are not useful for Zeeman measurements. For a magnetic field in the plane of the sky, the three Zeeman components are linearly polarized with the π component parallel to and the σ components perpendicular to the magnetic field direction. For a magnetic field along the line of sight, $I_\pi = 0$ and the I_σ are oppositely circularly polarized. If the magnetic field is parallel (antiparallel) to the direction of propagation of the radiation, $I_\sigma+$ is right (left) circularly polarized. In the general case of arbitrary angle θ between the line of sight and the magnetic field, the I_σ will be elliptically polarized. Generally $\nu_Z << \Delta\nu$ (the line width in frequency units), and it is not possible to infer complete information about **B** from Zeeman observations. Although the Stokes parameters V, Q, and U for the Zeeman components provide in principle full information about magnetic field strength and direction, in practice full information on **B** cannot be obtained owing to the extreme weakness of Q and U (typically about an order of magnitude weaker than V). The Stokes V spectra reveal the sign (i.e., direction) and magnitude of the line-of-sight component $B_{\rm los}$. That is, $V = (dI/d\nu)\nu_Z \cos\theta$. By fitting the frequency derivative of the Stokes parameter I spectrum dI/dν to the observed V spectrum, $B_{\rm los} = \nu_Z \cos\theta/Z$ may be inferred.

It is possible to correct statistically for the fact that only one component of **B** is measured, i.e., $B_{\rm los} = |\mathbf{B}| \cos\theta$. For a large number of clouds whose magnetic fields are randomly oriented with respect to the observed line of sight,

$$\overline{B}_{\rm los} = \int_0^{\pi/2} |\mathbf{B}| \cos\theta \sin\theta d\theta = \frac{1}{2}|\mathbf{B}|. \tag{2}$$

If **B** is strong, clouds will have a disk morphology with **B** along the minor axis. To properly measure λ, one needs B and N along a flux tube, i.e., parallel to the minor axis. As noted by Crutcher (1999), the path length through a disk will be too long by $1/\cos\theta$ and N (and M) will be overestimated, while $|\mathbf{B}|$ (and Φ) will be underestimated by $\cos\theta$. Again statistically,

$$\overline{M/\Phi} = \int_0^{\pi/2} \frac{M_{\rm obs}\cos\theta}{\Phi_{\rm obs}/\cos\theta} \sin\theta d\theta = \int_0^{\pi/2} (M/\Phi)_{\rm obs} \cos^2\theta \sin\theta d\theta = \frac{1}{3}(M/\Phi)_{\rm obs}. \tag{3}$$

The 1/3 correction factor is only appropriate for the strongly magnetized case, where clouds have a disk-like morphology. We will discuss λ_C obtained by applying this correction factor of 1/3 to the directly observed λ, since a disk morphology is the prediction of the ambipolar diffusion model; the 1/3 correction must be applied to test this model.

3.2 Dust polarization

Far-infrared and millimeter wavelength observations of linearly polarized dust emission may be used to map the morphology of the magnetic field projected onto the plane of the sky, $B_{\rm pos}$ (Hildebrand 1988). Linear polarization arises from elongated grains with their short axes aligned, generally with **B** (Lazarian 2003). The position angle of maximum emission will be perpendicular to $B_{\rm pos}$. However, it is not possible to measure directly the strength of $B_{\rm pos}$ since fairly weak magnetic fields can align grains, so the degree of polarization is not a measure of field strength.

In the early days of interstellar polarization studies, Chandrasekhar and Fermi (1953) suggested that analysis of the small-scale randomness of magnetic field lines could yield estimates of the field strengths. The method depends on the fact that turbulent motions will lead to irregular magnetic

fields (since under interstellar conditions fields will be frozen into the matter). There will therefore be a perturbed or MHD-wave component to the field that should show up as an irregular scatter in polarization position angles relative to those that would be produced by a regular magnetic field. The stronger the regular field, the more it resists being irregularized by turbulence. They showed that the magnitude of the irregularity of field lines could yield the regular field strength in the plane of the sky:

$$B_{\rm pos} = Q\sqrt{4\pi\rho}\,\frac{\delta V}{\delta\phi} \approx 9.3\sqrt{n(H_2)}\,\frac{\Delta V}{\delta\phi}\;\mu G, \tag{4}$$

where $\rho = mn(H_2)$ is the gas density, δV is the velocity dispersion, $\delta\phi$ is the dispersion in polarization position angles in degrees, Q is a factor of order unity, $n(H_2)$ is the molecular hydrogen density in molecules cm^{-3}, and $\Delta V = \sqrt{8ln2}\;\delta V$ is the FWHM line width in km s^{-1}. Here we have used $Q = 0.5$, a calibration based on study of simulations of interstellar clouds by Ostriker, Stone, and Gammie (2001), but see also Heitsch et al. (2001) and Padoan et al. (2001). These simulations found that this method could yield reliable results in molecular clouds if $\delta\phi < 25°$. One should note that while fluctuations in the field along the line of sight will be smoothed out by the polarization measurements, the calibration by the simulations referred to above include this in the Q factor. Heitsch et al. (2001) studied the effects of smoothing due to inadequate spatial resolution in the plane of the sky; although such smoothing will produce too large an estimate of $B_{\rm pos}$, the problem can be overcome so long as the region being studied, i.e. a molecular cloud or core, is adequately (a few resolution elements) resolved.

The Chandrasekhar-Fermi method of estimating B is a statistical one that may be in error by ~ 2 for an individual cloud. Also, similarly to Zeeman observations, in general N (and M) will be overestimated by $1/\cos\theta$ if the sight line has an angle θ to the minor axis, while $|\mathbf{B}|$ (and Φ) is underestimated by $\sin\theta$ (rather than by $\cos\theta$ in Zeeman observations). Again statistically,

$$\overline{M/\Phi} = \int_0^{\pi/2} \frac{M_{\rm obs}\cos\theta}{\Phi_{\rm obs}/\sin\theta}\sin\theta d\theta = \int_0^{\pi/2} (M/\Phi)_{\rm obs}\cos\theta\sin^2\theta d\theta = \frac{1}{3}(M/\Phi)_{\rm obs}. \tag{5}$$

So the correction factor is the same 1/3 as for the Zeeman case.

3.3 Spectral-line linear polarization

Linear polarization may also arise in radio-frequency spectral lines formed in the interstellar medium, even when Zeeman splitting is negligible. This Goldreich-Kylafis effect (Goldreich and Kylafis 1981; Kylafis 1983) may be used to probe magnetic field morphologies in molecular clouds. The direction of the polarization can be either parallel or perpendicular to the magnetic field, depending on the relationship between the line of sight, the direction of the magnetic field, and the direction of a velocity gradient that produces the anisotropic line optical depth that is required to produce linear polarization. Although the theory makes specific predictions for whether the field is parallel or perpendicular to the line polarization, in general the observations do not provide all of the necessary information. This ambiguity is unfortunate, but if structure in a cloud causes a flip by 90° in the polarization direction, it would easily be recognized and not confused with random magnetic fields. It therefore is a valuable tool in the measurement of magnetic field direction and in the degree of randomness of the field. As is the case for dust polarization, the Chandrasekhar-Fermi method may be applied to maps of spectral-line linear polarization to estimate field strengths.

3.4 Faraday rotation

Faraday rotation produces a rotation of the position angle of linearly polarized radiation; the rotation measure is given by

$$RM\ (\text{radian m}^{-2}) = \int_0^L B_{\rm los} n_e dx. \tag{6}$$

Because electron densities n_e and path lengths L for molecular clouds are small, RMs are generally dominated by the ionized diffuse interstellar medium, and Faraday rotation has not been thought to

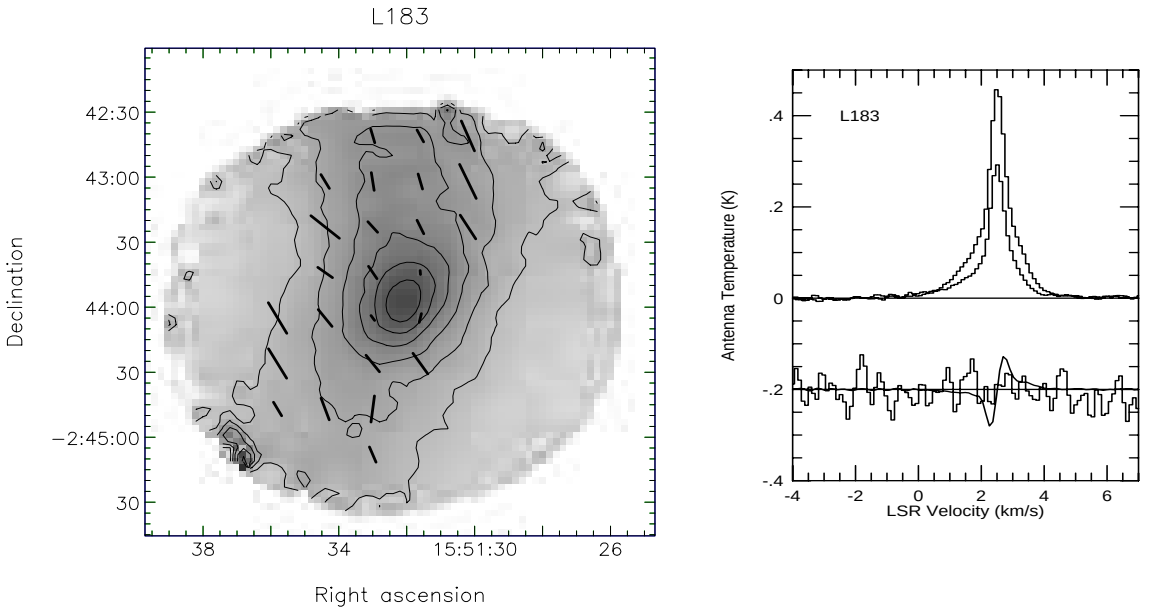

Fig. 1. Left: Dust polarization map of the starless core L 183. Grey-scale and contours show the dust emission at 850 μm. Thick line segments show the direction of the magnetic field projected on the sky; lengths are proportional to the polarized flux. Right: OH 1665 and 1667 MHz line profiles toward L 183. Observed data are histogram plots; the fit to Stokes V in the lower panel is a line. Top panel shows the two Stokes I spectra. Bottom panel shows the mean Stokes V spectrum for the two lines with a $3-\sigma$ upper limit fit.

be a technique for studying magnetic fields in molecular clouds. However, Wolleben and Reich (this volume) have argued that depolarization of background synchrotron radiation that is observed at the boundaries of dark clouds in Taurus is due to a Faraday screen in the envelopes of these clouds. If confirmed by OH Zeeman observations, this technique would be very valuable in probing magnetic field strengths in molecular cloud envelopes.

4 Observational Results

It is not possible in the space available to discuss all of the observational results. Important examples of work that will not be discussed include that of Matthews, Wilson, and Fiege (2001), who investigated the possibility that helical fields may surround and constrain filaments, and of Houde et al. (2002), who applied a novel technique involving the difference in ionized and neutral molecular line widths to infer the angle of **B** to the line of sight. Here we describe three representative examples of the observational results: the low-mass starless core L 183, the young stellar system and molecular outflow NGC 1333 IRAS4A, and the high-mass star formation region DR 21 (OH).

4.1 L 183

Figure 1 shows observational results for the starless core L 183; the left panel shows the SCUBA dust emission and polarization map at 850 μm (Crutcher et al. 2004), while the right panel shows the NRAO 43-m telescope observation of Stokes I and V spectra of 18-cm OH lines (Crutcher et al. 1993). The dust polarization map has an angular resolution of $21''$ and covers $3'$; the observed dust polarization position angles have been rotated by 90° so the line segments are in the direction of $B_{\rm pos}$. The OH spectra were obtained with a telescope beam diameter of $18'$.

The dust polarization map samples the core of L 183, with a density of $n(H_2) \approx 3 \times 10^5$ cm^3. The magnetic field is fairly regular, in agreement with the field being strong enough to resist turbulent twisting. But the dispersion in position angles of 14° (corrected for measurement error) is significant,

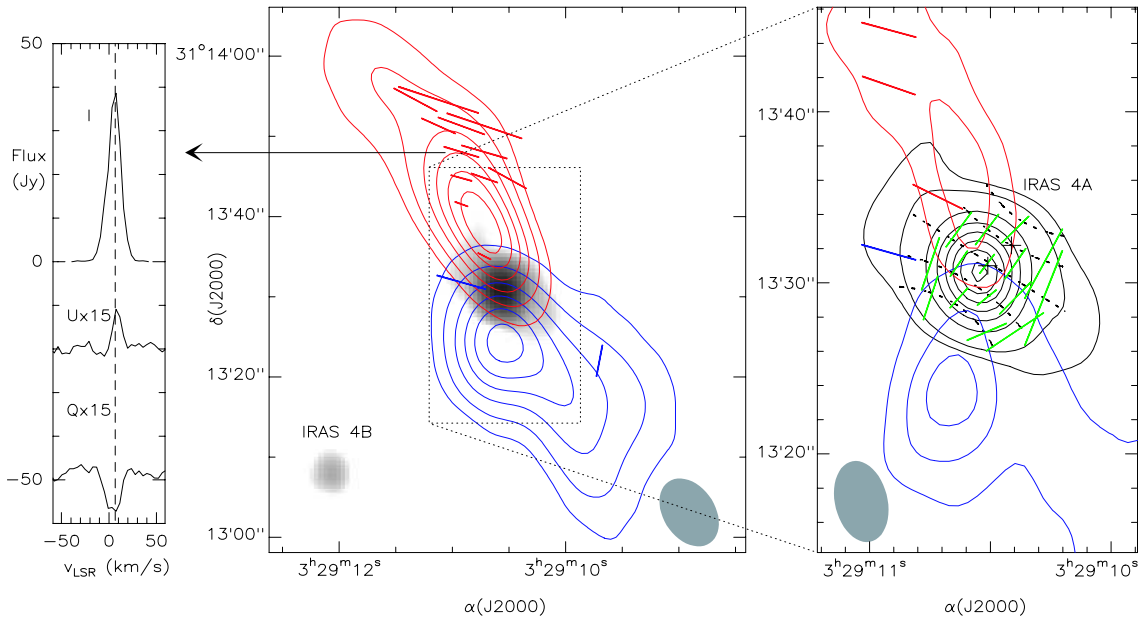

Fig. 2. BIMA observations of NGC 1333 IRAS4A. The middle panel shows dust emission (greyscale) and CO 2–1 redshifted (north lobe) and blueshifted (south lobe) emission from the bipolar outflow. Line segments superposed on the outflow show the polarization of the line emission. The mean Stokes I, U, and Q profiles for the redshifted lobe are shown in the left panel. The right panel shows the central region with thick contours showing dust emission, thin contours showing CO outflow, and black line segments showing CO polarization, and grey line segments showing the dust polarization. Dotted lines show a possible hourglass morphology for **B**.

implying that some turbulent twisting is present. The angle between the projected minor axis of the core and $\overline{B_{\rm pos}}$ is $\sim 30°$. The magnetic support model calls for the projected field to lie along the projected minor axis. Applying the Chandrasekhar-Fermi technique yields $B_{\rm pos} \approx 80\,\mu$G and $\lambda_C \approx 0.9$ for the dense core. Hence, the mass-to-flux ratio is approximately critical, in agreement with the magnetic support model. The OH Zeeman spectra sample a much larger area – the extended envelope of the L 183 core, for which $n(H_2) \approx 1 \times 10^3$ cm^3. The Zeeman effect is not detected to a $3-\sigma$ upper limit of $B_{\rm los} < 16\,\mu$G, which implies $\lambda_C > 0.5$ for the envelope. This limit is consistent with the envelope being subcritical, which is required by the magnetic support/ambipolar diffusion model.

4.2 NGC 1333 IRAS4A

NGC 1333 IRAS4A is a very young low-mass star formation region with multiple young stellar systems and an associated molecular outflow. Figure 2 shows BIMA observations (Girart, Crutcher, and Rao 1999) of the dust and CO outflow emission and polarization at 1.3 mm. The line polarization is perpendicular to the dust polarization. In the outflow, where the direction of the velocity gradient is known, it is possible to predict theoretically that the line polarization should be parallel to $B_{\rm pos}$ and therefore perpendicular to the dust polarization, as observed. The outflow is initially north-south, at about a 50° angle to $B_{\rm pos}$. A successful theory of molecular outflows must account for such a difference between **B** and the outflow. However, about 25″ from the center the difference is only 15°, suggesting that the field has deflected the outflow. The morphology of the dust polarization is suggestive of a pinched or hourglass morphology, in agreement with the predictions o f a strong magnetic field.

4.3 DR 21 (OH)

Figure 3 shows results for the high-mass star formation region DR 21 (OH); the left panel shows the BIMA dust and CO emission and polarization map at 1.3 mm (Lai, Girart, and Crutcher 2003), while

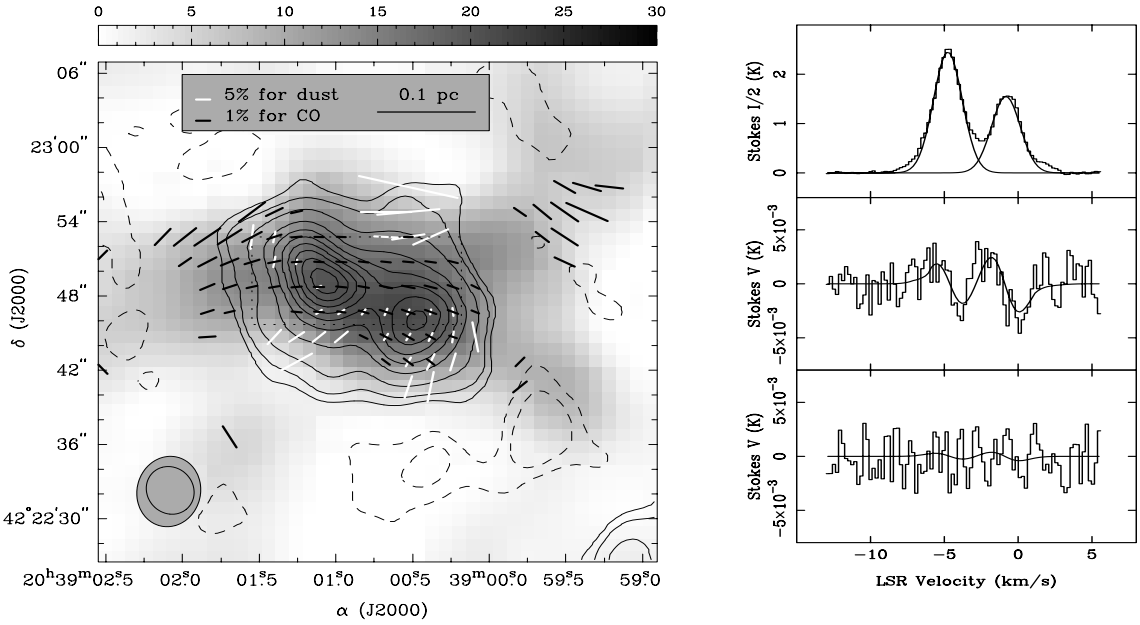

Fig. 3. Left: BIMA map of the high-mass star formation region DR 21 (OH). Contours show the 1.3-mm dust emission, grey scale shows the CO 2–1 line emission integrated over velocity, white line segments show the dust polarization, and black line segments show the CO linear polarization. Right: CN 1–0 line profiles toward DR 21 (OH). Observed data are histogram plots, fits are lines. Top panel shows the Stokes I spectrum with two Gaussians fitted. Middle panel shows the mean Stokes V spectrum for the four hyperfine components that have strong Zeeman splitting coefficients Z; the bottom panel shows the three components with weak Z. $B_{\rm los}$ was fitted independently for the two Gaussian lines.

the right panel shows IRAM 30-m telescope Stokes I and V spectra of the 3-mm CN lines (Crutcher et al. 1999). In millimeter-wave dust emission the main component of DR 21 (OH) consists of two compact cores (Woody et al. 1989) with a total mass of ~ 100 M$_\odot$. The two CN velocity components are each centered on a different one of the two compact cores. The region has associated masers of OH (Norris et al. 1982), H_2O (Genzel and Downes 1977), and CH_3OH (Batrla and Menten 1988), and high-velocity outflows powered by the two compact cores (Lai, Girart, and Crutcher 2003). The results from the dust and CO 2–1 linear polarization maps suggest that the magnetic field direction in DR 21 (OH) is parallel to the CO polarization and therefore parallel to the major axis of DR 21 (OH). This could be explained by a toroidal field produced by rotation of the double core. The strong correlation between the CO and dust polarization suggests that magnetic fields are remarkably uniform throughout the envelope and the cores. Both the dust emission and the CN lines sample a density $n(H_2) \approx 1 \times 10^6$ cm^3. The Chandrasekhar-Fermi technique yields an estimate of the magnetic field strength in the plane of the sky of about 1 mG, compared with about 0.5 mG inferred for the line-of-sight field from the CN Zeeman detection. Combining these results, the total field strength $|\mathbf{B}| \approx 1.1$ mG and $\mathbf{B}$ is at an angle $\theta \sim 60°$ to the line of sight. Then $\lambda_{\rm obs} \approx 1.0$. Since we know θ, we need not make a statistical correction to $\lambda_{\rm obs}$ but may find the correct λ_C; the result is $\lambda_C \approx 0.5$, or subcritical. However, uncertainties in $B_{\rm pos}$ and in $B_{\rm los}$ are sufficiently large that θ is quite uncertain.

5 Test Results

Although we have only discussed results for three molecular clouds, they are good exemplars for the available data, all of which are considered here in applying the three tests described in §2.

5.1 Morphology

Maps of dust and spectral-line linear polarization and of the Zeeman effect generally show a regular field morphology (e.g., Figures 1, 2, and 3), and an hourglass morphology is sometimes seen (e.g.,

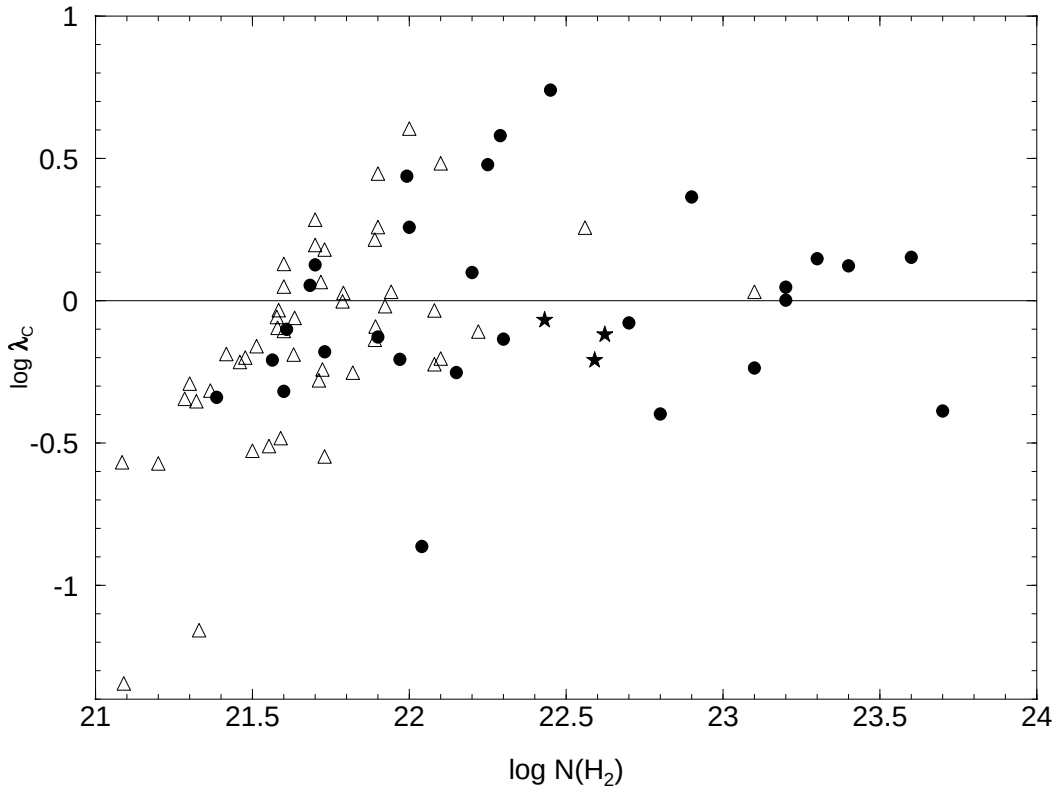

Fig. 4. λ_C are the observed mass to magnetic flux ratios, divided by 3 to correct for projection bias, in units of the critical values. $\lambda_C > 1$ is supercritical, $\lambda_C < 1$ is subcritical. Dots are for Zeeman data with $B_{\rm los} > 3\sigma(B_{\rm los})$, stars are for Chandrasekhar-Fermi estimates of $B_{\rm pos}$, and triangles are lower limits plotted at $B_{\rm los} = 3\sigma(B_{\rm los})$. Although the statistical correction of 1/3 for geometrical bias has been applied to each point, so that statistically this plot should be valid, for any individual point the true λ could be higher or lower than the plotted λ_C. A large part of the scatter in Figure 4 may therefore be due to geometrical projection effects.

Figure 2; see also Schleuning 1998). A regular field dominating a random field and an hourglass morphology toward cores are predictions of the strong magnetic field model. However, **B** projected onto the sky is not observed to be parallel to the minor axes of starless cores as predicted by magnetic support (e.g., Figure 1). Finally, even though fairly small, the dispersion in polarization position angles is often greater than observational errors (e.g., Figure 1), implying that turbulence is producing an irregular component to **B**.

5.2 Scaling

At low densities $n \sim 0.1 - 100$ cm^{-3}, it has been clear for some time that there is no correlation of $|\mathbf{B}|$ with ρ (Troland and Heiles 1986). At higher densities one finds $|\mathbf{B}| \propto \rho^{\kappa}, \kappa = 0.47 \pm 0.08$ (Crutcher 1999). Basu (2000) showed that a better correlation was obtained by fitting $|\mathbf{B}|$ *vs.* $\sigma\sqrt{\rho}$ (see his figure 1). Both the turbulence and magnetic support models predict little or no correlation between $|\mathbf{B}|$ and ρ at low densities, as observed. At higher densities, both paradigms predict $\kappa \approx 0.5$, so this does not discriminate between the two models. However, $|\mathbf{B}| \propto \sigma$ is a prediction of some turbulent support of clouds.

5.3 Mass-to-flux ratio

Figure 4 shows all of the λ_C available from Zeeman detections and sensitive limits for molecular clouds (Crutcher 1999; Bourke et al. 2001; Troland and Crutcher 2004), plus the Chandrasekhar-Fermi results

for three prestellar cores (Crutcher et al. 2004). The observations are distributed roughly equally above and below the $\lambda_C = 1$ line that divides subcritical and supercritical M/Φ ratios for disk geometries. Therefore, the data suggest that $\overline{\lambda} \approx 1$; that is, the typical mass to magnetic flux ratio is approximately critical. There is a slight indication that for large column densities, $\overline{\lambda}$ may be supercritical, and for small column densities, subcritical.

It is also relevant to consider mass-to-flux ratios in H I clouds, from which molecular clouds presumably form. Heiles and Troland (2004) have carried out an extensive study with the Arecibo telescope of Galactic H I clouds (for which $n(\mathrm{H\,I}) \sim 50$ cm^{-3}) in absorption against background extragalactic continuum sources (see also Troland, this volume). Their plot of $B_{\rm los}$ *vs.* $N(\mathrm{H\,I})$ showed that for all of the detections, the field was significantly subcritical. Moreover, almost all of the non-detections were also consistent with $\lambda < 1$. If these points were to be plotted on Figure 4, they would lie to the left of and below the $\lambda_C = 1$ line (see Troland, this volume). Hence, the H I data suggest that the precursors to molecular clouds are subcritical, as required by the magnetic support model.

In the ambipolar diffusion model the envelopes of dark clouds are the regions where λ remains essentially unchanged while ambipolar diffusion drives M/Φ supercritical in the core. Hence, envelopes of dark clouds provide a crucial test of magnetic support models – M/Φ *must* be subcritical in these regions. Dark-cloud envelopes were observed by Crutcher (1993); the result was $\overline{\lambda} \approx 1-2$, rather than the $\lambda < 1$ required by magnetic support. However, the observations had poor angular resolution ($18'$) with no mapping; these and other effects may have biased the results to larger λ. The Faraday screen (Wolleben and Reich, this volume) estimates of $B_{\rm los} \approx 20$ μG in the envelopes of Taurus dark clouds would certainly imply subcritical mass-to-flux ratios, as required by the magnetic support model.

6 Conclusions

The generally regular morphology of polarization maps supports a strong magnetic field model. Yet the small-scale scatter in polarization position angles predicted by turbulence is seen, although this scatter is generally relatively small. As projected onto the sky, **B** is not parallel to the minor axes of cores, as predicted by the magnetic support model. A triaxial cloud morphology, due perhaps to formation by compressible turbulence, can account for this (Basu 2000). The observation that $|\mathbf{B}| \propto \sigma$ is a prediction of a turbulent component of the support of clouds. The observations of molecular cloud cores are consistent with $\lambda \approx 1$. This is certainly inconsistent with the extreme turbulent model with negligible **B**, for which $\lambda >> 1$. Although $\lambda \approx 1$ is predicted to occur in cores as a result of ambipolar diffusion when the original mass-to-flux ratio was subcritical, the observational evidence for subcritical clouds and especially for subcritical envelopes is weak. Whether λ is slightly greater than or slightly less than 1 is crucial for whether magnetic fields provide support that is removed by the action of ambipolar diffusion. The present data are not sufficiently accurate to discriminate between these cases since λ in molecular clouds is observed to be (frustratingly) close to 1.

It seems that the data remain inconclusive in deciding between the two extreme models for what drives star formation. However, the fact that the regular component of **B** seems to dominate the irregular component and that mass-to-flux ratios are approximately critical ($\lambda \approx 1$) rather than the highly supercritical ($\lambda >> 1$) values predicted by weak field models provides strong support for the strong magnetic field model. A hybrid paradigm may be closest to the truth. In such a paradigm, compressible turbulence dominates in the diffuse ISM over both gravity and magnetic fields, sometimes forming self-gravitating clouds. The residual effects of this turbulence are seen in self-gravitating molecular clouds, but such clouds appear to be primarily magnetically supported. In any case, it is clear that *both* turbulence and strong magnetic fields are important in the physics of molecular clouds.

As is often the case in astronomy, further observations are needed. Tests of the role of magnetic fields are of necessity statistical in nature and must involve data covering a wide range of physical parameters. Required are additional high sensitivity surveys of magnetic field strengths and other cloud properties in order to assess the relative importance of magnetic fields in molecular cores and envelopes. These surveys should include extended polarization maps that allow a determination of how the field in the cores connects with that in its surroundings. But the single most crucial observation that is needed is the measurement of magnetic field strengths in a statistically significant sample of

molecular cloud envelopes. If envelopes are subcritical, with a large sample at least some of the fields must be nearly along the line of sight, and Zeeman observations will detect unambiguous subcritical mass-to-flux ratios. Clear evidence for an increase in the mass-to-flux ratio from envelope to core would then verify the ambipolar diffusion model. Alternatively, if future observations show that this is not found, turbulence driven star formation (although with dynamically important magnetic fields) would be favored. As has been the case in the last few years, future telescopes and instruments will enable ever more sensitive and extensive observations that hopefully will define more precisely the role of magnetic fields in the star formation process.

Acknowledgments

This work was partially supported by NSF grant AST 02-05810. I thank Tom Troland for an enjoyable and productive collaboration on the study of interstellar magnetic fields.

References

Basu, S. (2000) *Astrophys. J.* **540**, L103.
Batrla, W., Menten, K.M. (1988) *Astrophys. J.* **329**, L117.
Bourke, T.L., Myers, P.C., Robinson, G., Hyland, A.R. (2001) *Astrophys. J.* **554**, 916.
Chandrasekhar, S., Fermi, E. (1953) *Astrophys. J.* **118**, 113.
Crutcher, R.M., Troland, T.H., Goodman, A.A., Heiles, C., Kazès, I., Myers, P.C. (1993) *Astrophys. J.* **407**, 175.
Crutcher, R.M., Troland, T.H., Lazareff, B., Paubert, G., Kazès, I. (1999) *Astrophys. J.* **514**, L121.
Crutcher, R.M. (1999) *Astrophys. J.* **520**, 706.
Crutcher, R.M., Nutter, D., Ward-Thompson, D., Kirk, J.M. (2004) *Astrophys. J.*, in press.
Elmegreen, B.G. (2000) *Astrophys. J.* **530**, 277.
Genzel, R., Downes, D. (1977) *Astron. Astrophys. Suppl.* **30**, 145.
Girart, J.M., Crutcher, R.M., Rao, R. (1999) *Astrophys. J.* **525**, L109.
Goldreich, P., Kylafis, N.D. (1981) *Astrophys. J.* **243**, L75.
Heiles, C., Troland, T.H. (2004) *Astrophys. J.*, to be submitted.
Heitsch, F., Zweibel, E.G., MacLow, M.-M., Li, P.S., Norman, M. L. (2001) *Astrophys. J.* **561**, 800.
Hildebrand, R.H. (1988) Quar. Jour. Roy. Ast. Soc. **29**, 327.
Houde, M., Bastien, P., Dotson, J.L., Dowell, C.D., Hildebrand, R.H., Peng, R., Phillips, T.G., Vaillancourt, J.E., Yoshida, H. (2002) *Astrophys. J.* **569**, 803.
Kylafis, N. D. (1983) *Astrophys. J.* **275**, 135.
Lai, S.-P., Girart, J.M., Crutcher, R.M. (2003) *Astrophys. J.*, in press.
Lazarian, A. (2003) J. Quant. Spec. and Rad. Tran. **79-80**, 881.
Matthews, B.C., Wilson, C.D., Fiege, J.D. (2001) *Astrophys. J.* **562**, 400.
Mouschovias, T.Ch., Ciolek, G.E. (1999) in *The Origin of Stars and Planetary Systems*, eds. C. J. Lada, N. D. Kylafis, Kluwer, p. 305.
Nakano, T., Nakamura, T. (1978) Publ. Astron. Soc. Jap. **30**, 681.
Norris, R.P., Booth, R.S., Diamond, P.J., Porter, N.D. (1982) *Mon. Not. R. Astron. Soc.* **201**, 191.
Ostriker, E.C., Stone, J.M., Gammie, C.F. (2001) *Astrophys. J.* **546**, 980.
Padoan, P., Goodman, A., Draine, B.T., Juvela, M., Nordlund, Å., Rögnvaldsson, Ö.E. (2001) *Astrophys. J.* **559**, 1005.
Schleuning, D.A. (1998) *Astrophys. J.* **493**, 811.
Troland, T.H., Heiles, C. (1986) *Astrophys. J.* **301**, 339.
Troland, T.H., Crutcher, R.M. (2004) *Astrophys. J.*, to be submitted.
Woody, D.P., Scott, S.L., Scoville, N.Z., Mundy, L.G., Sargent, A.I., Padin, S., Tinney, C.G., Wilson, C.D. (1989) *Astrophys. J.* **337**, L41.

"The Magnetized Interstellar Medium"
8–12 September 2003, Antalya, Turkey
Eds.: B. Uyaniker, W. Reich & R. Wielebinski

Collapse of Interstellar Molecular Clouds

Dicle Zengin, E. Rennan Pekünlü and Esra Tiğrak

University of EGE, Faculty of Science, Department of Astronomy & Space Sciences,
35100 Bornova - Izmir, Turkey

Abstract. In this paper we systematically investigate the length and time scales of an interstellar molecular cloud for collapse under the influence of self-gravity and magnetic field forces. We used Magnetohydrodynamic (MHD) equations in linearized form in order to explore the dynamical evolution of perturbations. We found that the Lorentz force supports the cloud against self-contraction, i.e., the Lorentz force introduces stabilizing effect against gravitational instability. Of the two cloud types with the same physical size, only those threaded by an interstellar magnetic field will survive against gravitational collapse.

1 Introduction

Giant Molecular Clouds (GMCs) in the Milky way and in other galaxies are believed to be the birth places of stars. A widely accepted view is that portions of molecular clouds go through gravitational collapse and initiate star formation. But, there is yet to be found actual kinematic evidence of collapse. It is essential to test the theoretical pictures with observational data. Some of the models, such as the "inside-out collapse model" (Shu, 1977; Shu et al., 1987), make testable predictions about the density and velocity fields. Testing these predictions in simple clouds like small globules is a prerequisite for comprehending star formation in more massive clouds.

Early optical studies based on star count techniques showed that many small globules have central density structures (Bok & McCarthy, 1977; Tomita et al., 1978). These findings supported an early suggestion that gravitational collapse is going on in these globules (Bok & Reilly, 1947). Martin & Barrett (1978) suggested that molecular line studies indicate that some globules were unstable against gravitational collapse. Far infrared observations of B335 revealed direct evidence of star formation in this widely studied globule (Keene et al., 1983). The IRAS data base has provided more evidence for star formation in globules (Clemens et al., 1990; Yun & Clemens, 1990).

Typical masses of molecular clouds are in the range 10^3–10^4 $M_\odot$: If these were free falling, their lifetimes would have been unrealistically short, and the implied star formation rate would be much higher than observed (Zuckerman & Palmer, 1974; Mouschovias, 1976). There must be some force or forces supporting these clouds against their self-gravity. Thermal pressure forces alone cannot support these clouds against their self-gravity, for Bonnor–Ebert ($\simeq$ Jeans) critical mass is typically less than 10 $M_\odot$ at the observed low temperatures (see Crutcher et al. 1994). Supersonic turbulence may be regarded as another mechanism supporting larger masses. And it is certainly true. However, supersonic turbulence dissipates on such a short time scale compared to cloud lifetimes to be of significance (Crutcher, 1994). Magnetic fields, no matter how weak, have been shown to give support against gravity in dense, massive clouds (Mouschovias, 1976; Mouschovias & Spitzer, 1976; Spitzer, 1978; Mouschovias, 1987).

2 Self-Initiated Star Formation

We systematically present, with progressively more realistic physical inputs, the length and time scales of collapse in self-gravitating, isothermal, magnetically supported molecular clouds in its initial state. In subsection 2.1 we review the well-known cloud collapse by self-gravity alone. For homogeneous gas, an analysis due to J. H. Jeans can be found in Scheffler & Elsässer (1987). In subsection 2.2.

we investigate the more general problem of cloud collapse under the influence of self-gravity and the magnetic field. Summary and Conclusions are presented in Section 3.

2.1 Cloud Collapse by Self-Gravity

The dynamical evolution of the cloud is investigated by hydrodynamic equations (see, e.g. Scheffler & Elsässer, 1978). When linearized and assumed that the space and time variation of Fourier components of the perturbed quantities is of the form exp [i (ω t - k x)] for a one-dimensional case, the linearized hydrodynamic equations (1)–(4)

$$\frac{\partial \rho}{\partial t} + \nabla \cdot (\rho\, v) = 0 \tag{1}$$

$$\rho \frac{D\, v}{Dt} \equiv \rho \frac{\partial v}{\partial t} + \rho\, (v \cdot \nabla)\, v = -\nabla P - \rho \nabla \Phi \tag{2}$$

$$\nabla^2 \Phi = 4\pi \rho . G \tag{3}$$

$$P = c_s^2 \rho \tag{4}$$

yield the dispersion relation

$$\omega^2 = k^2 c_s^2 - 4\pi \rho_0 G\ , \tag{5}$$

where the symbols have their usual meanings. If there is to be self-gravity, then the perturbed mass density ρ_1 should grow in time. A necessary condition for this is $\omega^2 < 0$ which is equivalent to $k^2 < 4\pi\rho_0 G/c_s^2$. The threshold wave number k_g of the perturbation is defined as $4\pi\rho_0 G/c_s^2 = k_g^2$ (Scheffler & Elsässer, 1978). Thus the Jeans criterion for instability becomes

$$L_g > L_J = \sqrt{\frac{\pi c_s^2}{4\rho_0 G}} = \sqrt{\frac{\pi k_B T}{4\rho_0 G \bar{\mu} m_H}} = \frac{7.822}{\bar{\mu}} \sqrt{\frac{T}{N_H}} pc\ , \tag{6}$$

where L_J is often called the Jeans length, k_B is the Boltzmann constant, T is the temperature, N_H is the number density of H atoms, m_H is the proton mass, and $\bar{\mu}$ is the mean molecular weight.

2.2 Magnetized Cloud Collapse by Self-Gravity

Magnetic fields are shown to play a decisive dynamical role in regions of star formation (see McKee et al. (1993) for theoretical arguments and Heiles et al. (1993) for observational data). Magnetic fields support the clouds against gravitational contraction in two ways. One is the pressure of static magnetic field perpendicular to the field lines (Mouschovias & Spitzer, 1976). The other magnetic support mechanism involves fluctuating fields associated with MHD waves at sub-Alfvénic yet supersonic speeds. MHD waves may persist longer than purely hydrodynamic turbulence and support the cloud in both parallel and perpendicular (to magnetic field) directions (Crutcher, 1994). In this subsection we take the hitherto neglected Lorentz force into account and find the "modified" Jeans length. The linearized form of the equation of motion is:

$$\frac{\partial v_1}{\partial t} = -\frac{1}{\rho_0} \nabla P_1 - \nabla \Phi_1 - \frac{1}{8\pi\rho_0} \nabla B^2 + \frac{1}{4\pi\rho_0} (B \cdot \nabla)\, B\ , \tag{7}$$

We assume that the magnetic field is "frozen" into the gas. Only a critical ionization level can justify this assumption. With the assumption of the frozen-in condition, the magnetic induction equation can be written as

$$\frac{\partial B}{\partial t} = \nabla \times (v \times B)\ , \tag{8}$$

the linearized form of which is:

$$\frac{\partial B_1}{\partial t} = B_0 \cdot \nabla v_1 - B_0 \left(\nabla \cdot v_1\right) \ . \tag{9}$$

Linearized forms of equations (1), (3), (4), (7) and (9) form a closed set of equations. We may combine equations (1) and (9) to get the new form of the induction equation:

$$\frac{\partial B_1}{\partial t} = B_0 \cdot \nabla v_1 + \frac{B_0}{\rho_0} \frac{\partial \rho_1}{\partial t} \ . \tag{10}$$

We assume that $\mathbf{B} \cdot \nabla \mathbf{B} = \mathbf{0}$. This implies that, due to the absence of the mirror force, particles cannot accelerate in space along magnetic field lines. This fact in turn implies that $\mathbf{B_0} \cdot \nabla \mathbf{v_1} = \mathbf{0}$. Elimination of this term from equation (7) brings the induction equation into a new form:

$$\frac{\partial B_1}{\partial t} = \frac{B_0}{\rho_0} \frac{\partial \rho_1}{\partial t} \ . \tag{11}$$

Now, the dispersion relation we obtain is:

$$\omega^2 = \left(c_s^2 + \frac{B_0^2}{4\pi\rho_0} \right) k^2 - 4\pi\rho_0 G \ . \tag{12}$$

Equation (12) gives us the Jeans length L_{g+B}, where subscripts denote the presence of both the gravitational potential and the magnetic field:

$$L_{g+B} > \sqrt{\frac{\pi \left(c_s^2 + v_A^2\right)}{4\rho_0 G}} pc \ \ , \tag{13}$$

where $v_A = B_0/(4\pi\rho_0)^{1/2}$ is the Alfvén speed.

If we compare equations (6) and (13) we see that $L_{g+B} > L_g$. This comparison clearly shows that magnetized clouds are supported by magnetic field against collapse by self-gravity. Indeed, any initiation of self-contraction is resisted by magnetic pressure. In other words, of two interstellar clouds with exactly the same physical parameters, the one threaded by a uniform magnetic field requires greater dimensions (L) in order to collapse.

3 Summary and Conclusions

Molecular clouds with masses $\sim 10^3$–10^4 $M_\odot$ cannot go through free fall, otherwise the star-formation rate would be higher than observed. Forces resisting the initiation of self-contraction may be listed as thermal pressure forces which balance gravity along field lines, while magnetic and thermal pressure forces do so perpendicular to the field lines.

We reviewed the case in subsection 2.1. wherein self-gravity and thermal pressure forces determine the dynamical evolution of a cloud. Inclusion of Lorentz forces clearly showed that the magnetic pressure forces support the cloud against self-contraction. This fact manifested itself through the Jeans length. Comparison of marginal stability length scales showed that of two identical clouds the one threaded by a uniform magnetic field requires greater dimensions to collapse.

References

Bok, B. J., McCarthy, C. C. (1977) *Astron. J.* **79**, 42.
Bok, B. J., Reilly, E. F. (1947) *Astrophys. J.* **105**, 255.
Clemens, D., Yun, J., Heyer, M. (1990) *Astrophys. J. Suppl.* **75**, 877.
Crutcher, R. M. (1994) *ASP Conf. Series* **65**, 87.
Crutcher, R. M., Mouschovias, T. Ch., Troland, T. H., Ciolek, G. E. (1994) *Astrophys. J.* **427**, 839.

Heiles, C., Goodman, A. A., McKee, C. F., Zweibel, E. (1993) in *Protostars and Planets III*, eds. E. H. Levy & J. I. Lunine, (Tucson: Univ. Arizona Press), p. 279.
Keene, J. et al. (1983) *Astrophys. J.* **274**, L43.
Martin, R., Barrett, A. (1978) *Astrophys. J. Suppl.* **36**, 1.
McKee, C. F., Zweibel, E., Goodman, A. A., Heiles, C. (1993) in *Protostars and Planets III*, eds. E. H. Levy & J. I. Lunine, (Tucson: Univ. Arizona Press), p. 327.
Mouschovias, T. Ch. (1976) *Astrophys. J.* **206**, 753.
Mouschovias, T. Ch. (1987) in *Physical Processes in Interstellar Clouds*, eds. G. E. Morfill & M. Scholer, NATO ASI Ser. (Dordrecht: Reidel), p. 453.
Mouschovias, T. Ch., Spitzer, L. H. (1976) *Astrophys. J.* **210**, 326.
Scheffler, H., Elsässer, H. (1987) *Physics of the Galaxy and Interstellar Matter*, (Berlin: Springer-Verlag).
Shu, F. H. (1977) *Astrophys. J.* **214**, 488.
Shu, F. H., Adams, F. C., Lizano, S. (1987) *Ann. Rev. Astron. Astrophys.* **25**, 23.
Spitzer, L., Jr. (1978) *Physical Processes in the Interstellar medium*, (New York: Wiley).
Tomita, Y. et al. (1978) *Publ. Astron. Soc. Japan* **31**, 407.
Yun, J., Clemens, D. (1990) *Astrophys. J.* **367**, L73.
Zuckerman, B., Palmer, P. (1974) *Ann. Rev. Astron. Astrophys.* **12**, 279.

"The Magnetized Interstellar Medium"
8–12 September 2003, Antalya, Turkey
Eds.: B. Uyanıker, W. Reich & R. Wielebinski

Influence of the Diamagnetic Effect on Magnetorotational Instability in Accretion Disks

Ebru Akbaş and E. Rennan Pekünlü

University of EGE, Faculty of Science, Department of Astronomy & Space Sciences,
Bornova, 35100, İzmir, Turkey

Abstract. The diamagnetic effect in protostellar accretion disks modifies slightly the magnetorotational instability which exists in the presence of Hall electromotive force. We have shown that inclusion of magnetization into the governing MHD equations does not change the unstable character of the disk but causes the wavelength range of the unstable mode to expand towards the shorter values.

1 Introduction

Before the 1990s, it was already realized that molecular viscosity was not enough to provide enhanced outward angular momentum transport in accretion disks. Shakura & Sunyaev (1973) conjectured that the Maxwell stress could ensue the onset of turbulence in accretion disks.

Balbus & Hawley (1991) showed that a weak magnetic field with a good frozen-in condition destabilizes an accretion disk with a Keplerian velocity profile. Under these conditions, the outcome is determined by the competition between the stabilizing Coriolis force and destabilizing magnetic tension force.

If the disk's magnetic field is weak, i.e. subthermal, then perturbations cause the growth of an unstable mode. The so-called slow mode is locally unstable, non-propagating (evanescent), independent of the magnetic topology of the disk and grows extremely rapidly. The intensity of the magnetic field is amplified 3–4 orders of magnitude in such a short time as a few orbital periods. Of many other proposed instabilities none can supply such a rapid growth. This is what happens in the linear regime.

Later, Balbus & Hawley (1992a, 1992b), Balbus et al. (1996), Hawley & Balbus (1991, 1992), Hawley et al. (1994), and Stone et al. (1996) studied the the evolution of the MRI in the non-linear regime. Computer simulations showed that the instability grows into a turbulence and a disk dynamo sets in, i.e., where magnetic field amplification is sustained in the presence of dissipation mainly by reconnection. From then on, Maxwell stresses which are 3–4 times higher than the Reynolds stresses provide the necessary anomalous viscosity which would trigger the enhanced outward angular momentum transport; this, in turn, causes accretion to take place.

This physically well-established instability is claimed to be so general that it has been shown to be applicable to all kind of Keplerian disks, be it as it may in CVs, YSOs or AGNs.

Later Balbus & Terquem (2001) investigated the MRI in the presence of the Hall effect in protostellar disks. Inclusion of the Hall e.m.f. into the calculations introduces a new feature, i.e., whatever the velocity profile, accretion disks are always unstable in the presence of a weak magnetic field.

But, especially in protostellar disks which are cool and dense, the frozen-in condition, in full radial extent of the disk, becomes questionable. Only the electrons in the hotter inner region may fulfil this condition.

However, Balbus & Terquem (2001) pointed out that electron–ion inductive coupling and ion–neutral collisional coupling together ensure the involvement of the bulk of the fluid. But this is still a delicate theoretical challenge which requires further investigation in YSOs and DNs.

Our analysis is partly, not wholly, the extension of Balbus & Terquem (2001) wherein the linear stability of a protostellar disk in the presence of a vertical magnetic field is analyzed and the importance

of the new feature, that is Hall e.m.f., is emphasized. In this study we extend Balbus & Terquem (2001). In protostellar disks, as we have already mentioned, the magnetic field is assumed to be frozen-in electron fluid only. This implies that there is no difference between the bulk velocity of electrons and the velocity of magnetic field lines. However, electrons gyrate around the field lines. The gyrating electrons generate an additional magnetic field (counterfield). This field opposes the external field threading the disk. The diamagnetic effect may be local as well as global in the disk. Local or global, diamagnetic currents are border-line cases. That is there appears a region, the width of which is of the order of an electron Larmor radius, within which the magnetic field intensity is weaker than outside. Thus our analysis has considered the hitherto neglected magnetization effect.

The diamagnetic effect or magnetization is defined as the magnetic moment, $\mu = mv_{\perp}^2$, per unit volume. As is apparent from the definition of the magnetic moment, the diamagnetic effect is proportional to B^{-1}. A weaker magnetic field, a prerequisite for the onset of the MRI, is made weaker by the diamagnetic effect. In this process, the effective value of the magnetic field and the energy density of the plasma are related, not independent quantities.

2 MRI in the presence of diamagnetism

As we have already pointed out above that the present investigation is the extension of Balbus & Terquem (2001), the interested reader should refer to the quoted reference for details. For the sake of completeness we reproduce the governing MHD equations and the equation for diamagnetism:

$$\frac{\partial \rho}{\partial t} + \nabla \cdot (\rho \mathbf{v}) = 0 \tag{1}$$

$$\rho \frac{\partial \mathbf{v}}{\partial t} + (\rho \mathbf{v} \cdot \nabla)\, \mathbf{v} = -\nabla \left(P + \frac{B^2}{8\pi} \right) - \rho \nabla \Phi + \left(\frac{\mathbf{B}}{4\pi} \cdot \nabla \right) \mathbf{B} \tag{2}$$

$$\frac{\partial \mathbf{B}}{\partial t} = \nabla \times \left(\mathbf{v} \times \mathbf{B} - \eta \nabla \times \mathbf{B} - \frac{c\,(\nabla \times \mathbf{B}) \times \mathbf{B}}{4\pi e n_e} \right) \tag{3}$$

$$\mathbf{J}_{mag} = c \nabla \times \mathbf{M} \tag{4}$$

If $\mathbf{H}$ were the magnetic field value in the absence of any magnetization effects, then the actual macroscopic field $\mathbf{B}$ in the region is given by Bodo et al. (1992):

$$\mathbf{B} = \mathbf{H} + 4\pi \mathbf{M} = \mathbf{H} - \frac{4\pi}{3} W_k \frac{\mathbf{B}}{B^2} \mathbf{H} - \frac{1}{6} \frac{W_k}{W_B} \mathbf{B} = \mathbf{H} - \varepsilon \mathbf{B} \tag{5}$$

where $W_B = B^2/8$ and $W_k = nmv^2/2$ are the magnetic field and particle kinetic energy densities, respectively, and $\varepsilon = W_k/6W_B$. Equation (5) has a simple acceptable solution,

$$B = \frac{H}{2} \left(1 + \sqrt{1 - \frac{2}{3} W_k / \left(H^2/8\pi \right)} \right) \tag{6}$$

We consider the local stability of a differentially rotating disk threaded by a weak vertical field. We assume that finite resistivity and Hall currents are both present. We restrict ourselves to plane wave disturbances of the form $\exp(\omega, t)$; this form keeps the coefficients of the dispersion relation real. We work in the Boussinesq limit and use standard cylindrical coordinates (R, ϕ, z) with the origin at the disk center. Under these circumstances pressure, density, vertical velocity and vertical magnetic field perturbations all vanish. We solve the linearized equations for $\delta v_R, \delta v_\phi, \delta B_R, \delta B_\phi, \delta H_R$ and δH_ϕ, which yield the dispersion relation in terms of dimensionless quantities:

$$s^4 + \left[\bar{\kappa}^2 + 2X(1-\varepsilon)^2 + \left[\frac{d \ln \Omega^2}{d \ln R} + Y(1-\varepsilon) \right] \frac{Y}{4} (1-\varepsilon) \right] s^2$$

$$+\left[\bar{\kappa}^2\frac{Y}{4}(1-\varepsilon)+X(1-\varepsilon)^2\right]\left[\frac{d\ln\Omega^2}{d\ln R}+Y(1-\varepsilon)+X(1-\varepsilon)^2\right]=0 \tag{7}$$

where $s=\omega/\Omega;\ X=(kv_A/\Omega)^2;\ Y=(kv_H/\Omega)^2$. It is easily verifiable that at the maximum growth rate s_m- Oort A value, the partial differentiation of Eq. (7) with respect to X and Y gives the coupled equations:

$$s_m^2+X(1-\varepsilon)^2+\frac{1}{2}\frac{d\ln\Omega^2}{d\ln R}+\frac{Y}{8}(1-\varepsilon)(\bar{\kappa^2}+4)=0 \tag{8}$$

$$\frac{1}{4}\frac{d\ln\Omega^2}{d\ln R}(s_m^2+\bar{\kappa}^2)+\frac{X}{4}(1-\varepsilon)^2(\bar{\kappa}^2+4)+\frac{Y}{2}(1-\varepsilon)(s_m^2+\bar{\kappa}^2)=0 \tag{9}$$

We would like to draw the reader's attention to Eq. (7). When, may we call it the magnetization parameter, vanishes, the Balbus & Terquem (2001) result is recovered, as it should be. The graphical solution of this equation is given in Figures 1.

3 Conclusion

If the inner and hotter regions of protostellar disks are regions where frozen-in conditions prevail, at least for electrons, then it is shown that the diamagnetic effect modifies the wavelength range of the unstable mode. Instability keeps its presence but now, as conjectured by Balbus & Hawley (1991), due to the weakend magnetic field, the unstable mode appears at shorter wavelengths. As to whether it develops into a turbulence is yet to be seen by simulations.

References

Balbus S.A. & Hawley J.F. (1991) *Astrophys. J.* **376**, 214.
Balbus S.A. & Hawley J.F. (1992a) *Astrophys. J.* **392**, 662.
Balbus S.A. & Hawley J.F. (1992b) *Astrophys. J.* **400**, 610.
Balbus S.A. , Hawley J.F. & Stone J. M. (1996) *Astrophys. J.* **467**, 76.
Balbus S.A. & Terquem C. (2001) *Astrophys. J.* **552**, 235.
Bodo G., Ghisellini G. & Trussoni E. (1992) *Mon. Not. R. Astron. Soc.* **255**, 694.
Hawley J.F. & Balbus S.A. (1991) *Astrophys. J.* **376**, 223.
Hawley J.F. & Balbus S.A. (1992) *Astrophys. J.* **400**, 595.
Hawley J.F., Gammie C.F. & Balbus S.A. (1995) *Astrophys. J.* **440**, 742.
Stone J.M., Hawley J.F., Gammie C.F. & Balbus S.A.. (1996) *Astrophys. J.* **463**, 656.
Shakura N.I. & Sunyaev R.A. (1973) *Astron. Astrophys.* **24**, 337.

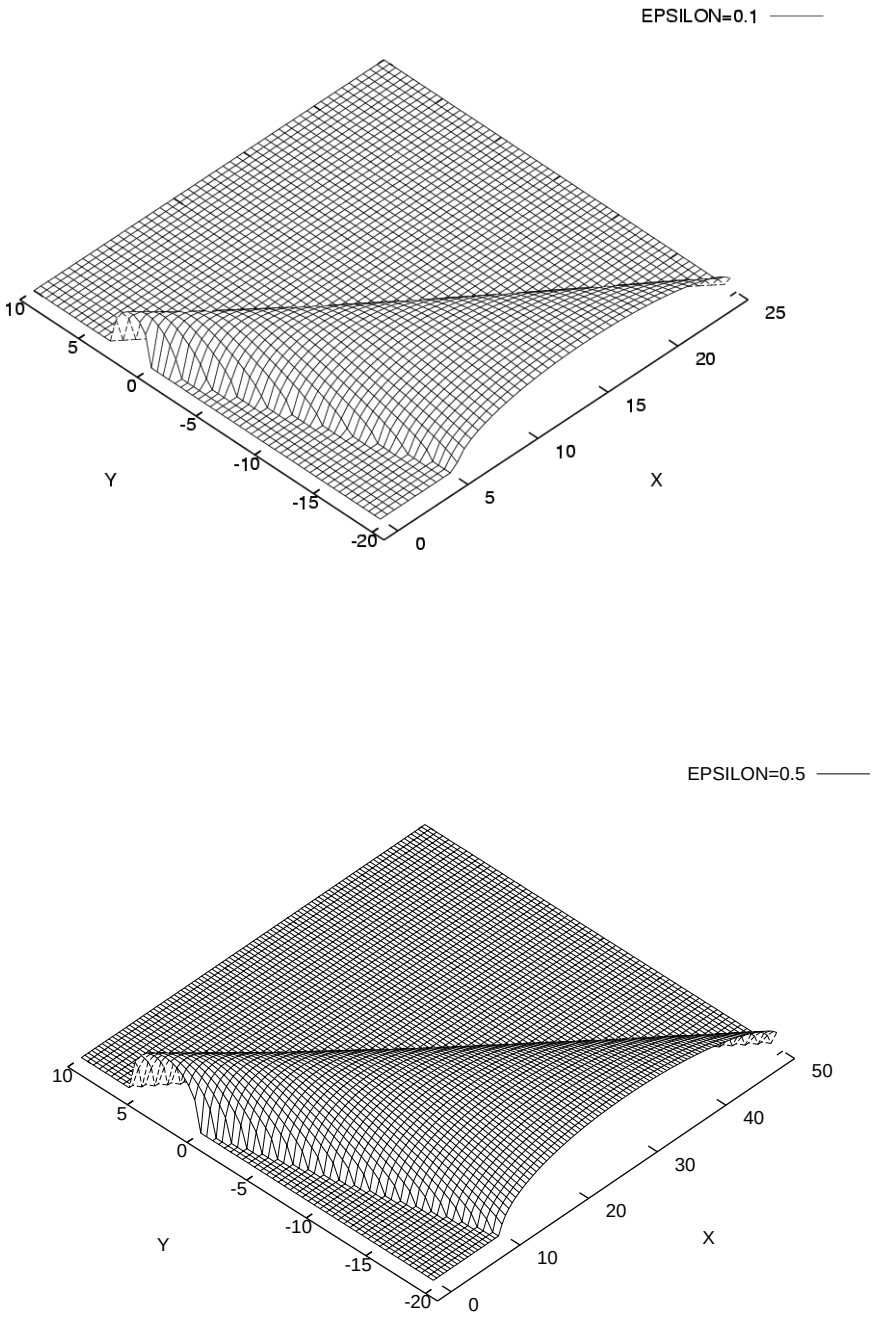

Fig. 1. Growth rate in the X, Y plane for $\eta = 0$ Keplerian disk. Only regions of instability are shown, with the height proportional to the growth rate. The vertical axis has been suppressed, but the maximum growth rate of the ridge is 0.75Ω. For weak magnetization, i.e. $\varepsilon = 0.1$; for strong magnetization, i.e. $\varepsilon = 0.5$. When compared with the Balbus & Terquem (2001) result, one can easily see that the ridge is shifted towards higher X and Y values which in essence measure the wave numbers of the unstable mode.

"The Magnetized Interstellar Medium"
8–12 September 2003, Antalya, Turkey
Eds.: B. Uyaniker, W. Reich & R. Wielebinski

Magnetic Fields in Supernova Remnants*

Ernst Fürst and Wolfgang Reich

Max-Planck-Institut für Radioastronomie, Auf dem Hügel 69, 53121 Bonn, Germany

Abstract. Observations of the polarized radio emission from supernova remnants are reviewed. Some characteristics of the deduced intrinsic magnetic fields are listed and used to determine the role of the magnetic field for the dynamics of these objects. The relation between the magnetic fields of SNRs and the Galactic magnetic field local to the SNRs is considered. Typical properties of the magnetic field of the various SNR classes are discussed. Recent results of OH Zeeman splitting observations indicate milli-Gauss magnetic fields in filamentary structures.

1 Introduction

Shortly after the proposal of synchrotron emission to be the source of the radio radiation from the Milky way by Kiepenheuer (1950) the continuous light from the Crab nebula was explained as due to synchrotron radiation by Shklovsky (1953). The optical linear polarization was discovered by Dombrovsky (1954) and confirmed by Oort & Walraven (1956). Mayer, McCullough & Sloanaker (1957) detected linear polarization (magnetic fields) from the Crab nebula at radio waves. This early work marks the beginning of a great career of magnetic fields in supernova remnants (SNRs).

According to Woltjer (1962) the dynamical evolution of SNRs can be divided into several phases: the ejected mass dominates the swept-up mass (free expansion, $R_s \propto t$, where R_s is the distance of the shock from the explosion centre). In the next phase the swept-up mass is much larger than the ejected mass but the shock is still strong (Sedov or adiabatic phase, compression ratio 4, $R_s \propto t^{2/5}$). Later radiation losses are no longer negligible and the expansion is controlled by the internal pressure of the SNR ($R_s \propto t^{2/7}$). When the internal pressure is low, the expansion is controlled by the momentum of the SNR ($R_s \propto t^{1/4}$). Final is the phase of dissipation. This simple picture is modified in case the supernova explodes into a large hot wind bubble, which has been created by the progenitor star and/or if the supernova shock-wave interacts with molecular clouds. This contribution discusses the properties of magnetic fields in SNRs and their relation to the interstellar medium. Measurements of magnetic field distributions across SNRs are important to derive parameters of the dynamics of the shock, information on the post-shock gas, and the interacting molecular clouds.

2 Observations of magnetic fields

The radio flux density of the synchrotron emission from a SNR is proportional to $B_{\perp}^{\frac{\gamma+1}{2}}\ \nu^{\frac{-(\gamma-1)}{2}}$, where γ defines the energy distribution $E^{-\gamma}$ of the relativistic electrons. The synchrotron radiation is linearly polarized and the plane of the electric field vector is rotated during the propagation insides the SNR and the interstellar medium. This rotation is due to different refractive indices of the two circular components of a linearly polarized wave and is called *Faraday rotation*. The angle ψ of rotation is given by

$$\Psi(\mathrm{rad}) \ = \ RM(\mathrm{rad/m^2})\ \lambda(\mathrm{m})^2, \quad RM \ = \ 8.1\ 10^5 \int N(\mathrm{cm^{-3}})\ B_{\parallel}(\mathrm{G})\ dz(\mathrm{pc}) \qquad (1)$$

*Based on observations with the Effelsberg 100-m telescope operated by the Max-Planck-Institut für Radioastronomie (MPIfR), Bonn, Germany

where RM is called the rotation measure, N is the thermal electron density and $B_{\parallel}$ the magnetic field component along the line of sight. The effect of Faraday rotation can be inferred from radio maps observed at different frequencies. An example is shown in Fig. 1.

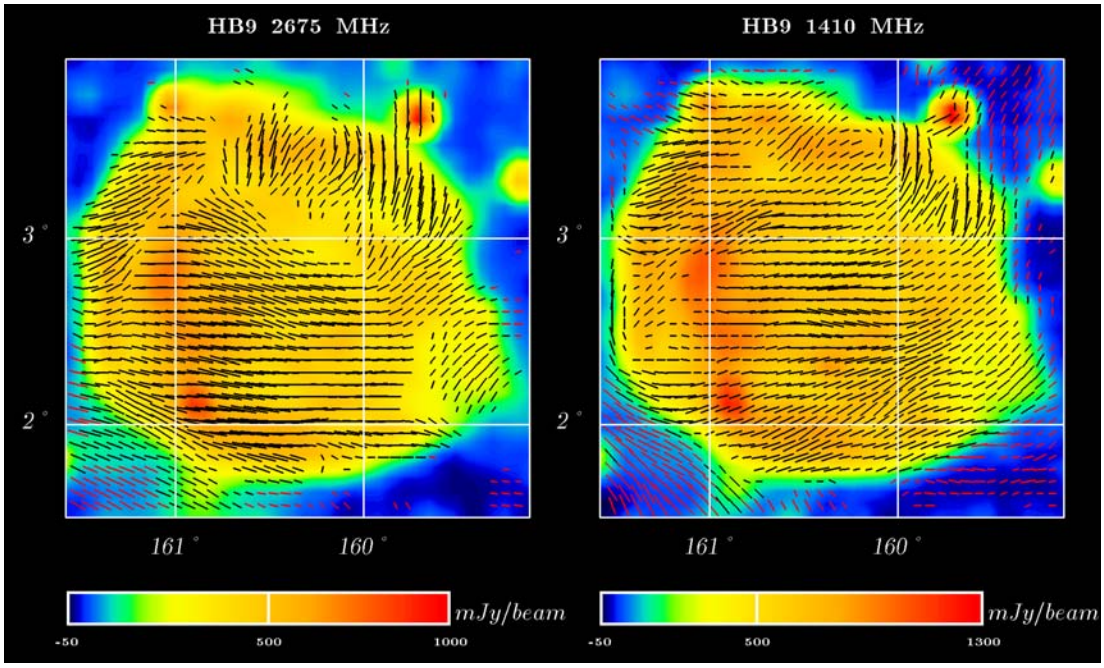

Fig. 1. The SNR HB9 at 2.7 GHz and 1.4 GHz observed with the Effelsberg 100-m telescope. Both maps have 9.′3 angular resolution. The bars denote the linear polarization (B-field). The length of the bars is proportional to the polarized intensity. Note that the vector difference at any given point in the two maps is due to Faraday rotation.

The variations of the electric field vectors in both maps can easily be verified. In principle, using the above equations, the intrinsic polarization angle can be calculated from $\Psi = \Psi_0 + RM \cdot \lambda^2$. Because of the ambiguity of a multiple of 180° concerning the measured value of Ψ should be read:

$$\Psi = \Psi_0 + RM \cdot \lambda^2 + n \cdot \pi \tag{2}$$

with $n = \pm 1, \pm 2, \ldots$

This ambiguity translates into a RM ambiguity:

$$RM = \frac{\Psi_1 - \Psi_2}{\lambda_1^2 - \lambda_2^2} + \frac{\Delta n \cdot \pi}{\lambda_1^2 - \lambda_2^2} \tag{3}$$

In general observations at three or more wavelengths are necessary to solve for the ambiguity. For the radio bands at 21 cm, 11 cm and 6 cm the corresponding ambiguities ($\Delta n = 1$) are $\Delta RM = 96$ rad/m^2 (21 cm/11 cm), $\Delta RM = 374$ rad/m^2 (11 cm/6 cm), and $\Delta RM = 76$ rad/m^2 (21 cm/6 cm). For the combination 11 cm/6 cm the ambiguity of RM is larger than typically observed rotation measures and in many cases the assumption of minimum rotation measure ($\Delta n = 0$) is reasonable for short-wavelength observations. If 21 cm wavelength is involved this assumption is often not valid. In Fig. 2 the intrinsic magnetic field distribution is shown based on a RM determination from observations at three frequencies.

Several attempts have been made to measure RMs using multi-channel polarimeters. At the Effelsberg 100-m telescope an eight-channel polarimeter for 21 cm wavelength has been recently installed. Each channel has a bandwidth of 4 MHz, the centre frequencies vary between 1388 and 1416 MHz. The ambiguity between adjacent channels is $\Delta RM > 10000$ rad/m^2, far beyond detected Galactic values. First results are discussed by Uyanıker (this volume).

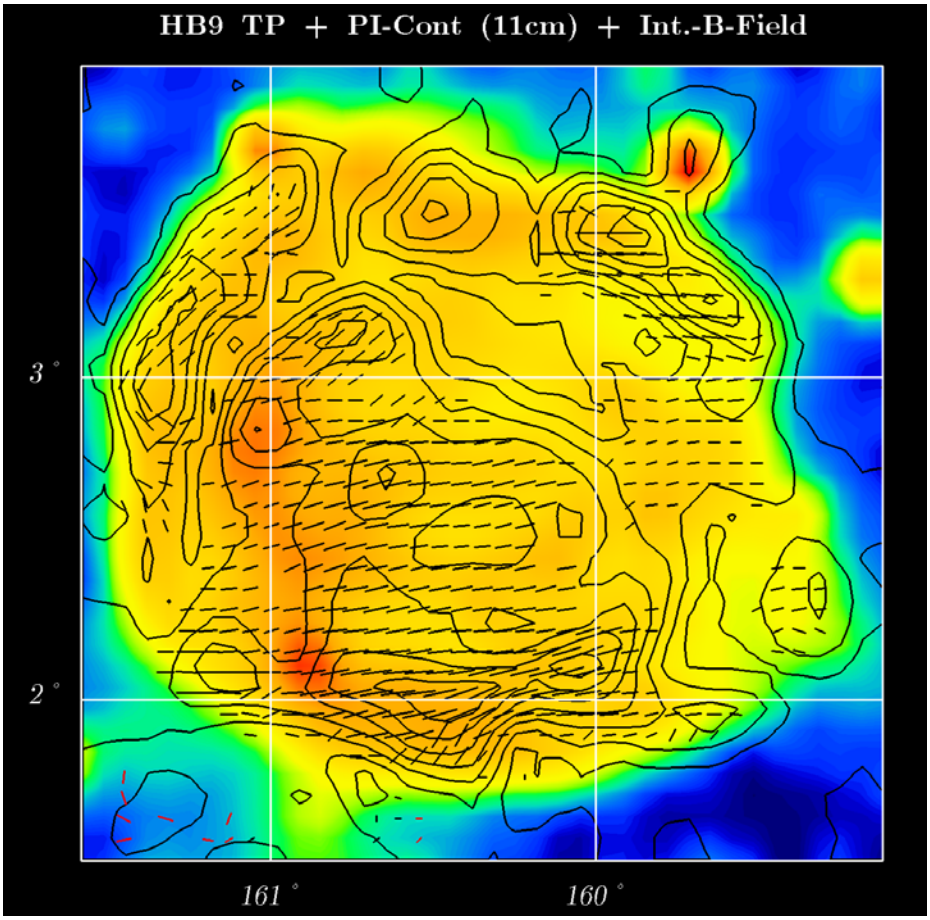

Fig. 2. The SNR HB9 at 2.7 GHz. The bars denote the magnetic field direction derived from observations at 1.4 GHz, 2.7 GHz and 4.8 GHz.

The observed fraction of polarization p is typically less, often much less, than the maximum possible value of about 70% to 75%. This is caused by depolarization, which may result if variations of the magnetic field occur on very small scales, i.e. within the antenna beam. Depolarization is also caused if Faraday rotation occurs along the line of sight, either internal or external to the radiating source (see Burn 1966, Sokolov et al. 1998).

3 Results

SNRs can be classified into three different groups. Young shell-type remnants (i.e. Tycho, SN1006, Kepler), evolved shells (i.e. G127.5−0.1, CTB1) and filled-centre SNRs (i.e. Crab, 3C58).

3.1 Young shells

The magnetic field in young supernova shells, which are often the remants of historical supernovae, is predominantly radially oriented. As an example Tycho is shown in Fig. 3. At higher angular resolution more details become visible on $1'$ to $2'$ scale (see observations of Tycho by Dickel 1990). The mean p for historical shell-type SNRs is between 4% and 15%, indicating a large fraction of random magnetic field. The most likely explanation of the radial magnetic field is based on Rayleigh-Taylor instabilities within the layer between the shock and the ejecta. The radial velocity component of these instabilities causes a stretching of the magnetic field.

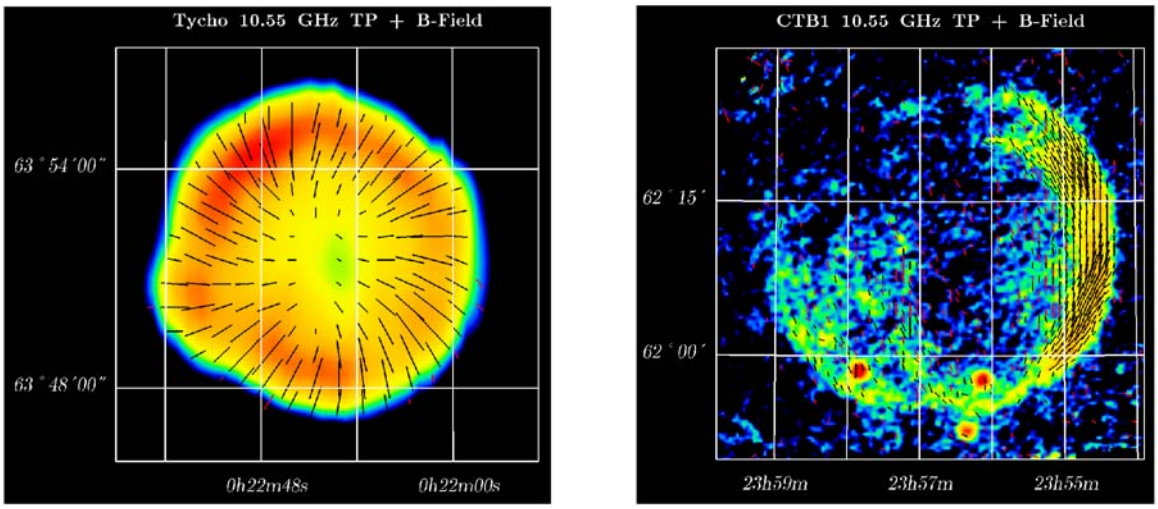

Fig. 3. Tycho's SNR and CTB1 at 10.55 GHz as observed with the Effelsberg 100-m telescope. Total intensity and polarization vectors in B-field direction are shown.

3.2 Evolved shells

Evolved shells show magnetic fields which are largely tangential to the shock front (see CTB1, Fig. 3). According to van der Laan (1962) the compression of the frozen-in interstellar magnetic field plays an important role. This leads to some alignment with the Galactic magnetic field local to the SNR. This alignment has been studied for a small sample of so-called bilateral symmetric SNRs (Fig. 4) by Fürst & Reich (1990), who find a good correlation between the geometrical axis of the SNRs and the magnetic field direction obtained from linear polarization measurements of stars (Mathewson & Ford 1971). A more extensive study has been made by Gaensler (1998), who investigated the correlation with the Galactic plane for 17 bilateral SNRs. For the majority of bilateral SNRs the angle between the symmetry axis of the SNRs and the Galactic plane is small, but a few deviations exist up to almost 90°. To establish the interpretation of the bilateral symmetry as a tracer of the ambient magnetic field more detailed data on magnetic fields local to the SNRs would be helpful.

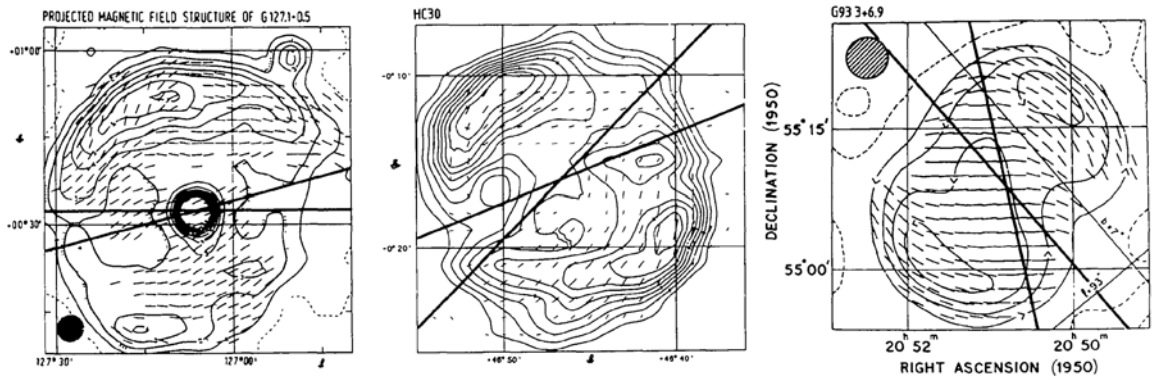

Fig. 4. Comparison of the symmetry axis of bilateral SNRs with the magnetic field direction local to the SNR (see Fürst & Reich (1990) for details). Such observations can be used to trace the Galactic magnetic field directions in distant spiral arms.

3.3 Filled-centre SNR

Several filled-centre SNRs have been observed with the Effelsberg 100-m telescope at 32 GHz with an angular resolution of 26″ (Reich 2002). At this angular resolution the magnetic field structure varies between radial (G21.5−0.9) and very patchy (3C58). Observations of the Crab nebula at higher angular resolution (Bietenholz & Kronberg 1990) show small-scale coherent magnetic structures of 10″ size. At least in some outer regions the magnetic field runs radial, perhaps caused by an outflow of charged particles from the central pulsar. The maximum polarization (at a beam of 1.″8) is about 65% indicating a well-ordered magnetic field on small scales.

4 The magnetic field strength

4.1 Minimum energy – Equipartition

Generally, the magnetic field strength is determined assuming the total energy of electrons, protons and the magnetic field to be minimum. Assuming a flux density spectral index of $\alpha = -0.5$ ($S_\nu \propto \nu^\alpha$) the minimum magnetic field is given by

$$B_{\min} \approx 10 \cdot \Phi^{-2/7} \cdot R\,(\mathrm{deg})^{-6/7} \cdot d\,(\mathrm{kpc})^{-2/7} \cdot S_{1\mathrm{GHz}}\,(\mathrm{Jy})^{2/7} \tag{4}$$

where Φ the relative radiating volume of the source, R ist the radius, d the distance, and S the flux density at 1 GHz (based on Pacholczyk 1970). For Tycho we obtain a magnetic field of about 0.2 mG, for G127.1+0.5 about 12 μG, which is in agreement with the adiabatically shock compressed interstellar magnetic field (van der Laan 1962).

4.2 The OH-line

With the rediscovery of the ground-state satellite line of the hydroxyl molecule (OH) at 1720.53 MHz as a tracer for SNR–molecular cloud interaction by Frail et al. (1994) measurements of the Zeeman splitting of this line has become an appropriate tool to measure the magnetic field in the SNR post-shock gas. About 20 SNRs are known to have associated OH-masers. For 10 SNRs the magnetic field has been derived (Sgr A East, W44, W28, G32.8−0.1, G346.6−0.2, W51C, G349.7+0.2, CTB37A, CTB33, and G357.7−0.1). The magnetic field parallel to the line of sight following from these observations lies in the range between a few tenths and a few milli-Gauss. In case of the SNR W44 a post-shock magnetic field of 0.28 mG was detected by Claussen et al. (1997). This small-scale magnetic field corresponds to a magnetic pressure of $B^2/8\pi \approx 3 \cdot 10^{-9}$ dyne cm^{-2}. This value has to be compared with the ram pressure of $\rho v^2 \approx 2 \cdot 10^{-7}$ dyne cm^{-2} derived from infrared observations of OI (Reach & Rho 1996) and the thermal pressure inside the remnant of $6 - 8 \cdot 10^{-10}$ dyne cm^{-2} (from X-ray, Rho et al. 1996). The magnetic field begins to play a considerable role on both local dynamics and structure of the shock. In case of W51C (Brogan et al. 2000) the magnetic pressure in the post-shock gas is even a factor of 100 larger.

4.3 Is the magnetic field dynamically important?

The magnetic field is unlikely to be dynamically important at least during the early phases. This can be demonstrated using the ratio R_H between the magnetic and the dynamic pressure. $R_H = \frac{B^2}{4\pi} / \frac{1}{2}\rho_1 v_s^2$ where ρ_1 is the upstream gas density and v_s is the shock velocity. For an interstellar magnetic field of 3 μG, an interstellar number density of 0.1 cm^{-3} and a shock velocity of 300 km s^{-1} the ratio R_H becomes about 0.01. Therefore, the magnetic field B plays a passive role. During the radiation phase the compression in the post-shock region (filaments) may be of order 100 larger giving a magnetic field strength of 1 mG. In that case the post-shock gas is controlled by the magnetic field.

During the interaction of the supernova shock wave with ambient molecular clouds heat conduction plays a significant role: The cloud may be heated up and evaporated increasing the density interior to the SNR. The evaporation rate depends on the temperature gradient: $\frac{dQ}{dt} = \mathrm{K\ grad\ T}$, where Q is

the heat quantity and K the heat conduction coefficient. The ratio K_{th} for a thermal plasma with no magnetic field and K_{gp} for a plasma with magnetic field (gyrotropic) is:

$$K_{th}/K_{gp} \approx 10^{10}\ T(\mathrm{K})^3\ B(\mathrm{G})^2\ n(\mathrm{cm}^{-3})^{-2}$$

(Spitzer 1962). Assuming a magnetic field B of 1 mG, a molecular cloud number density n of 1000 cm^{-3}, and a post-shock temperature T of 10000 K, the ratio is about 10^{10}. The magnetic field in the molecular cloud reduces the heat conduction significantly, the evaporation is much slower and the cloud may be further compressed to possibly form a new star.

5 Concluding remarks

Magnetic fields in SNRs provide information on the interaction of the supernova ejecta with the interstellar medium. Although in most cases dynamically unimportant, the magnetic field may control the expansion in filamentary structures, where the magnetic fields reach local values of up to a few milli-Gauss. The intrinsic magnetic field of SNRs shows typical characteristics depending on the type of SNRs. Young shells have typically radially directed magnetic field lines, while evolved shells show tangential fields caused by the interaction with the ambient gas. Future work on magnetic fields of SNRs may benefit from large-scale polarization surveys and the determination of Galactic magnetic structures (Reich et al., this volume).

References

Bietenholz M.T., Kronberg P.P. (1990) *Astrophys. J.* **357**, L13.
Brogan C.L., Frail D.A., Goss W.M., Troland T.H. (2000) *Astrophys. J.* **537**, 875.
Burn B.J. (1966) *Mon. Not. R. Astron. Soc.* **133**, 67.
Claussen M.J., Frail D.A., Goss W.M., Gaume R.A. (1997) *Astrophys. J.* **489**, 143.
Dickel J.R. (1990) in *Galactic and Intergalactic Magnetic Fields*, eds. R. Beck, P.P. Kronberg & R. Wielebinski, IAU Symp. 140, p. 76.
Dombrovsky V.A. (1954) *Doklady Akad. Nauk. SSSR* **94**, 1021.
Frail D.A., Goss W.M., Slysh V.I. (1994) *Astrophys. J.* **424**, L111.
Fürst E., Reich W. (1990) in *Galactic and Intergalactic Magnetic Fields*, eds. R. Beck, P.P. Kronberg & R. Wielebinski, IAU Symp. 140, p. 73.
Gaensler B.M. (1998) *Astrophys. J.* **493**, 781.
Kiepenheuer K.O. (1950) *Phys. Rev.* D **79**, 738.
Mathewson D.S., Ford V.L. (1971) *Mem. R. Astron. Soc.* **74**, 139.
Mayer C.H., McCullough T.P., Sloanaker R.M. (1957) *Astrophys. J.* **126**, 468.
Oort J.H., Walraven T. (1956) *B.A.N.* **12**, 285.
Pacholczyk A.G., (1970) *Radio Astrophysics*, W.H. Freemann and Company, San Francisco, p. 171.
Reach W.T., Rho J.H. (1996) *Astron. Astrophys.* **150**, L277.
Reich W. (2002) in *Neutron Stars, Pulsars, and Supernova Remnants*, Proc. 270. WE-Heraeus Seminar, eds. W. Becker, H. Lesch, & J. Tümper, MPE Report **278**, p. 1.
Rho J.H., Petre R., Pisarski R., Jones L.R. (1996) in *Röntgenstrahlung from the Universe*, eds. H.U. Zimmermann, J.E. Trümper & H. Yorke, MPE Report **263**, p. 273.
Shklovsky I.S. (1953) *Doklady Akad. Nauk. SSSR* **90**, 983.
Sokolov D.D., Bykov A.A., Shukurov A. et al. (1998) *Mon. Not. R. Astron. Soc.* **299**, 189.
Spitzer L. (1962) *Physics of fully ionized gases*, John Wiley, New York.
van der Laan H. (1962) *Mon. Not. R. Astron. Soc.* **124**, 125.
Woltjer L. (1972) *Annnu. Rev. Astron. Astrophys.* **10**, 129.

"The Magnetized Interstellar Medium"
8–12 September 2003, Antalya, Turkey
Eds.: B. Uyanıker, W. Reich & R. Wielebinski

Polarized Emission from Optical Filaments in Two Low Surface Brightness Supernova Remnants

Aylin Yar-Uyanıker[1,2], Bülent Uyanıker[1,2], and Roland Kothes[2,3]

[1] Max-Planck-Institut für Radioastronomie, Auf dem Hügel 69, 53121 Bonn, Germany
[2] National Research Council, Herzberg Institute of Astrophysics, Dominion Radio Astrophysical Observatory, P.O. Box 248, Penticton, B.C., V2A 6J9 Canada
[3] Department of Physics and Astronomy, The University of Calgary, 2500 University Dr. NW, Calgary, AB, T2N 1N4 Canada

Abstract. We report the detection of polarized radio emission from the partial optical shells of the two supernova remnants G114.3+0.3 and G116.5+1.1. The existence of coinciding optical and polarized emission implies that these parts of the SNRs are further developed. Highly polarized radio emission is a measure of the homogeneity of the magnetic field. Therefore, in these regions the magnetic field should be more regular in comparison to the unpolarized parts of the shell, where turbulent magnetic fields are expected.

1 Introduction

Low surface brightness supernova remnants (SNR) are difficult to detect, especially in polarization. If a SNR has a low surface brightness then usually little polarization is observed, because the SNR's polarization is coupled with the observed total intensity and does not exceed 70% of the total emission. This constraint, therefore, puts highly polarized SNRs of low surface brightness in a class of rare objects, since intervening interstellar material easily washes out this already weak emission by depolarizing it, leaving total emission intact. If, however, there are optically emitting regions in front of the remnant, and polarized emission can be detected in spite of this, then something is exceptional with the remnant or with the material in the line of sight: Either there is little or no depolarization or the remnant has an ordered magnetic field. The situation is even more difficult if the optical emission is physically associated with the polarized emission.

In this contribution, we present continuum images at 1.4 GHz towards the SNRs G114.3+0.3 and G116.5+1.1, taken from the Canadian Galactic Plane Survey (CGPS, Taylor et al. 2003), with an angular resolution of $49'' \times 49'' \ \mathrm{cosec}(\delta)$. Both of these remnants are of low surface brightness and partially polarized although there are associated optical filaments with them.

2 Observations

Recently the region towards $\ell = 115°$ has been discussed by Yar-Uyanıker et al. (2004) in the context of total intensity and H I emission to determine the distances of three SNRs in this area. They have discovered patches of H I emission surrounding G114.3+0.3 indicating a location in the Local arm at a distance of about 700 pc and suggest a possible relation between G116.5+1.1 and CTB 1, placing both remnants at a distance of about 1.6 kpc.

Figure 1 shows the total-intensity image of the area. Although CTB 1 has also associated optical filaments it is weakly polarized in our data. In the following sections we discuss the polarized and optical emission from G114.3+0.3 and G116.5+1.1.

2.1 G116.5+1.1

This remnant was discovered by Reich & Braunsfurth (1981) by its radio continuum emission. It is placed on top of a smooth emission plateau together with CTB 1. Optical filaments are detected

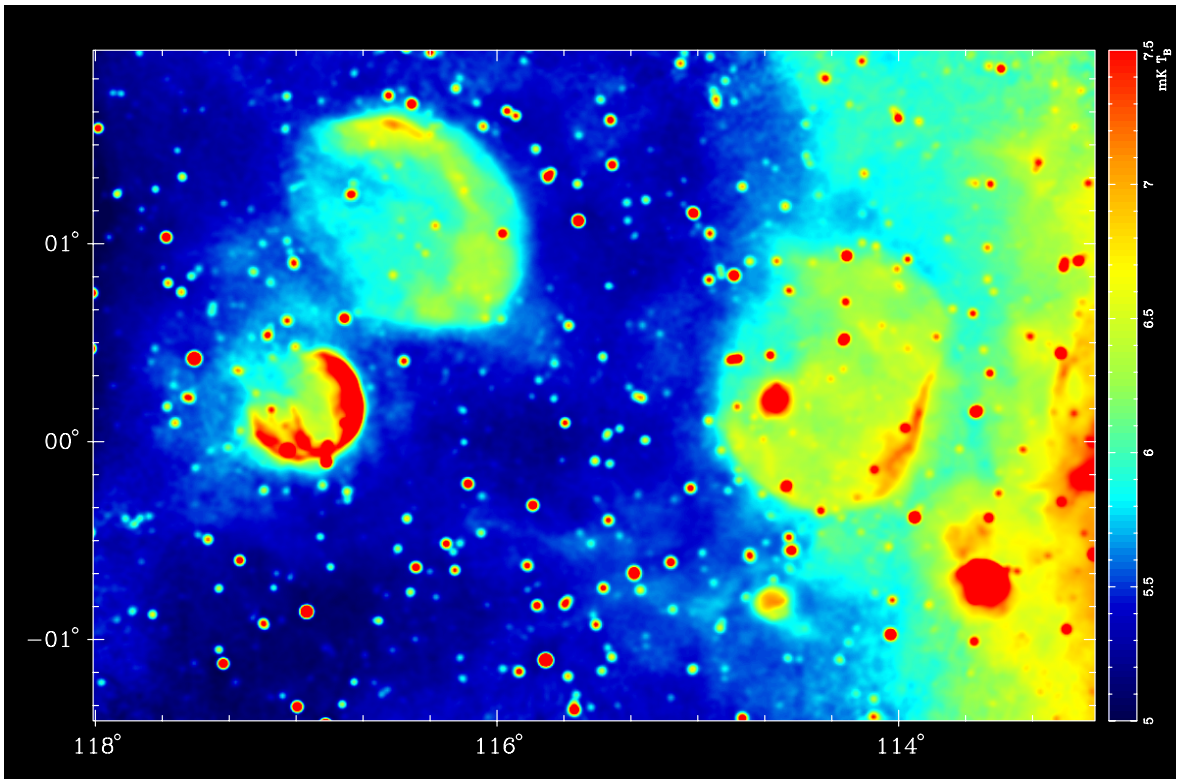

Fig. 1. Radio continuum image of the region covering the SNRs G114.3+0.3, G116.5+1.1, and G116.9+0.2 (CTB 1) at 1.4 GHz, observed with the DRAO Synthesis Telescope with large-scale structures added using the Effelsberg Survey data by Reich et al. (1997) at the same frequency.

towards this SNR by their Hα and S II emission (Fesen et al. 1997). A prominent filament, towards Galactic north, positionally coincides with the partial shell of high radio intensity. This coincidence suggests a relationship between radio and optical emission. This suggestion is further supported by the existence of S II emission, which is sensitive to density and is also considered as a good tracer of shocks.

We observe high percentage polarization in the western arc (up to 60%) just outside the total intensity shell (see Fig. 2). Tangential electric field vectors (not shown in the image) regularly follow the arc. Little depolarization effects favor a close distance (closer than 2 kpc due to the "polarization horizon" as described by Uyanıker et al. (2003)). A few faint optical filaments situated at the edge of the radio-bright northwestern limb of the SNR are detected in Hα ($\sim$100 km s^{-1}), S II and N II emission (Fesen et al. 1997). The most prominent one measures $\sim 30'$ in length. The Hα image of this filament is given in Fig. 3. The Hα/S II ~ 1 ratio implies an association between the filament and the SNR. S II emission indicates that the filament is formed due to the shock of the SNR. Optical measurements reveal an electron density of $n_e \sim 30$ cm^{-3} towards the remnant.

2.2 G114.3+0.3

This remnant was also discovered by Reich & Braunsfurth (1981) by its radio emission at 11 cm. Its angular size is $82' \times 65'$. Fürst et al. (1993) and Kulkarni et al. (1993) suggested an association between the SNR and the pulsar PSR 2334+61. The dispersion measure (DM) of the pulsar, 55$\pm$10 pc cm^{-3}, gives a distance of $\sim$2.4 kpc. However, Mitra et al. (2003) showed that this DM is affected by foreground H II emission and that the pulsar has an anomalous rotation measure (RM) behavior.

The polarized intensity image of the SNR is given in Fig. 4. The southern limb of the remnant is polarized with a percentage polarization varying between 10% and 20%. The electric field vectors are

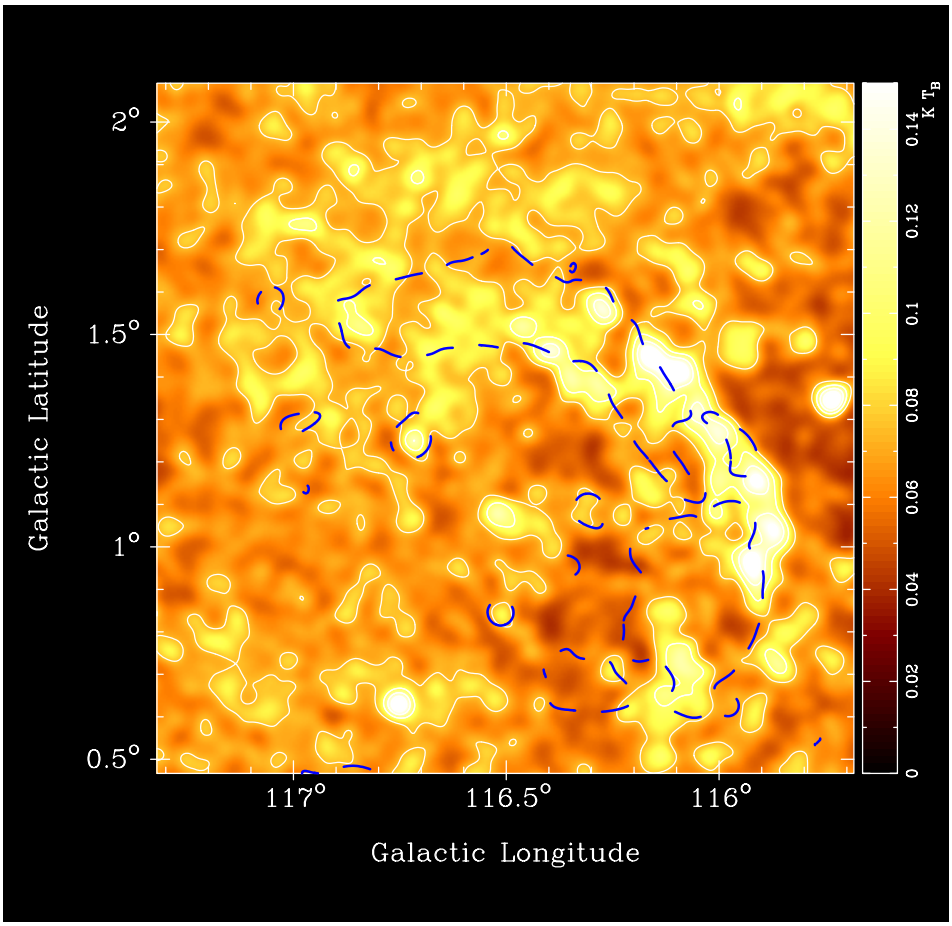

Fig. 2. Polarized intensity image of G116.5+1.1 as observed with the DRAO telescope. The dashed lines indicate the position of the total intensity emission.

regular and tangential in the south (not shown in the figure). An H II region (S 165 at 1.6 kpc) is seen within the SNR shell. S 165 does not cause any depolarization, therefore it should be located behind the remnant.

An Hα filament was observed towards the south of this SNR by Mavromatakis et al. (2002). The position of this filament is shown on the polarized intensity map in Fig. 5.

3 Results and discussion

The thin optical filaments coincide with polarized emission and are clearly associated with the SNRs, but they do not totally depolarize the SNRs. Tangential polarized emission implies regular magnetic fields and low turbulence in these regions. Optical images show that thermal electron densities towards these SNRs do not seem to vary much and can be considered as constant. The rotation in the plane of polarization due to Faraday rotation is

$$\Theta = 0.81\ n_{\rm e}\ B_{\parallel}\ \lambda^2\ L \qquad (1)$$

where Θ is the change in the polarization angle, $n_{\rm e}$ is the electron density, $B_{\parallel}$ is the parallel component of the magnetic field, λ is wavelength and L is the linear size of the Faraday active region. If $n_{\rm e}$ is more or less constant, is it possible to derive constraints on $B_{\parallel}$ or L on the basis of a regular magnetic field and for the case of small depolarization?

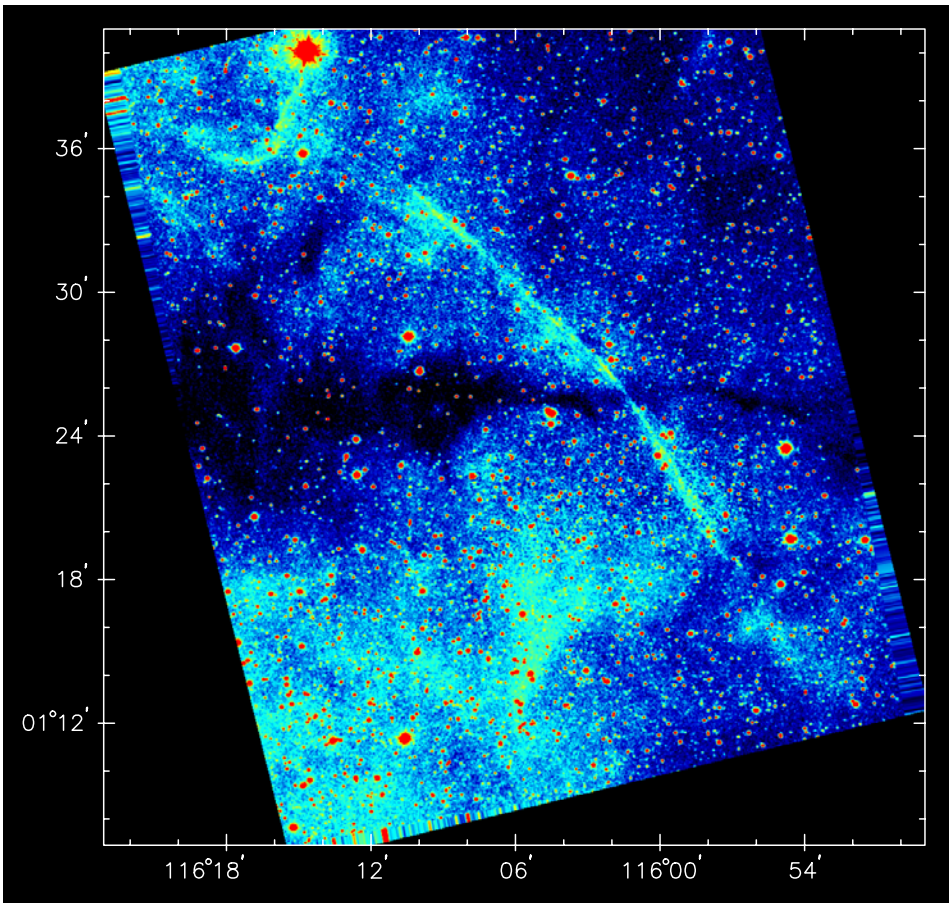

Fig. 3. Hα image of the optical filament towards the north of the SNR G116.5+1.1, observed by Fesen et al. (1997)

Across the prominent optical filament of G116.5+1.1 the electron density appears to be almost constant, $n_{\rm e} \sim 30$ cm^{-3}, and the magnetic field vectors are homogeneous with a maximum scatter of $\Delta\Theta \sim 30°$. Therefore, the thickness of the filament (L) and the strength of the magnetic field ($B_{\parallel}$) are the only parameters which can change the polarization angle, Θ. If we assume the filament is rope-like, then its thickness would be ∼0.46 pc. In this case the canonical interstellar magnetic field strength $B_{\parallel} \sim 2$ μG would alter the polarization angle by about $\Theta \sim 56°$, indicating that the magnetic field giving the observed polarization appearance is intrinsic to the remnant. Since we do not have any information at other wavelengths, we assume that the 30° variation in the polarization angle is the upper limit caused by the optical filament. This assumption alone allows us to calculate the strength of the parallel magnetic field component within the remnant. In order to deviate the polarization angle by $\Theta \sim 30°$ we need $B_{\parallel} \sim 1\,\mu$G.

For G114.3+0.3 we get a foreground dispersion measure of DM$_{\rm fore} = 13$ cm^{-3} pc, using the Taylor & Cordes (1993) model. But the pulsar has a dispersion measure of about 58 cm^{-3} pc. On the other hand, radio emission gives a very high RM of -100 rad m^{-2}, which combined with the pulsar DM leads to a foreground magnetic field parallel to the line of sight of $B_{\parallel} = 2.1$ μG. This is significantly higher than the expected value of $B_{\parallel} = 1$ μG (Mitra et al. 2003). The enhanced magnetic field indicates an additional structure along the line of sight with a strong magnetic field and high electron density causing the additional dispersion and rotation measure.

We now want to investigate the possibility that the shell of the expanding SNR itself causes the high RM and DM values. Assuming a foreground dispersion measure of DM$_{\rm fore} = 13$ cm^{-3} pc and a mean foreground magnetic field along the line of sight of $B_{\parallel} = 1$ μG, we get internal values of

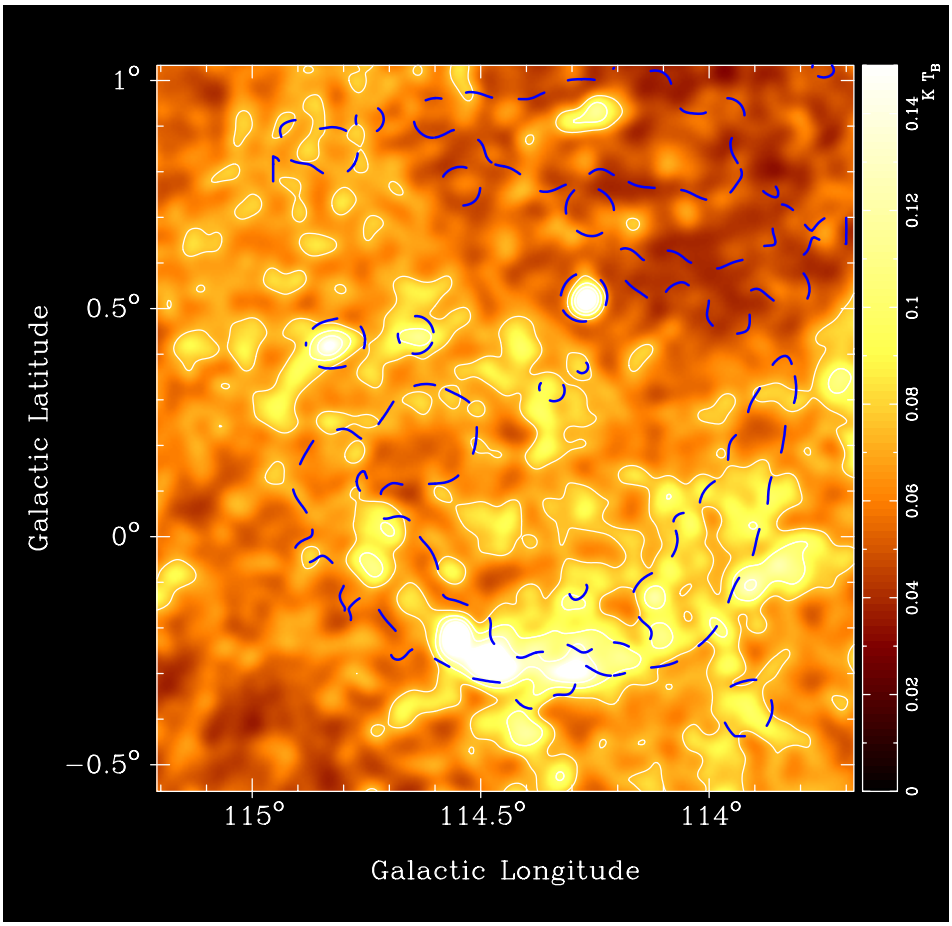

Fig. 4. Polarized intensity image of G114.3+0.3 as observed with the DRAO telescope. The dashed lines indicate the position of the total intensity emission.

$\mathrm{DM_{int}} = 45$ cm^{-3} pc, $\mathrm{RM^{int}} = -89$ rad m^{-2}, and $B_{\parallel}^{\mathrm{int}} = 2.4$ μG. We derive a compression ratio of 2.4. Assuming the same compression ratio for the interstellar material, swept up by the expanding shock wave and a radius of 7 pc, we get a width of 1.2 pc for the shell. Using the width and the internal DM, we found an electron density of 38 cm^{-3} within the shell. Assuming the swept-up material within the shell is fully ionized (H/He is 9:1) and again a compression ratio of 2.4, results in an ambient density of 14 atoms per cm^3, which is in accord with the observed H I density.

4 Conclusions

We have presented polarized images of two low surface brightness SNRs and reported on the detection of polarization towards the optical filaments in both of these SNRs.

For G116.5+1.1 we have calculated the strength of the parallel component of the magnetic field as $B_{\parallel} \sim 1$ μG, which is slightly less than the canonical interstellar magnetic field strength.

We also found that the expanding shell of G114.3+0.3 is responsible for the discrepancy in the observed RM and DM values. For this remnant we have calculated the magnetic field in the shell of the remnant as 2.4 μG.

Acknowledgments

We thank W. Reich for critical reading of the manuscript and discussions.

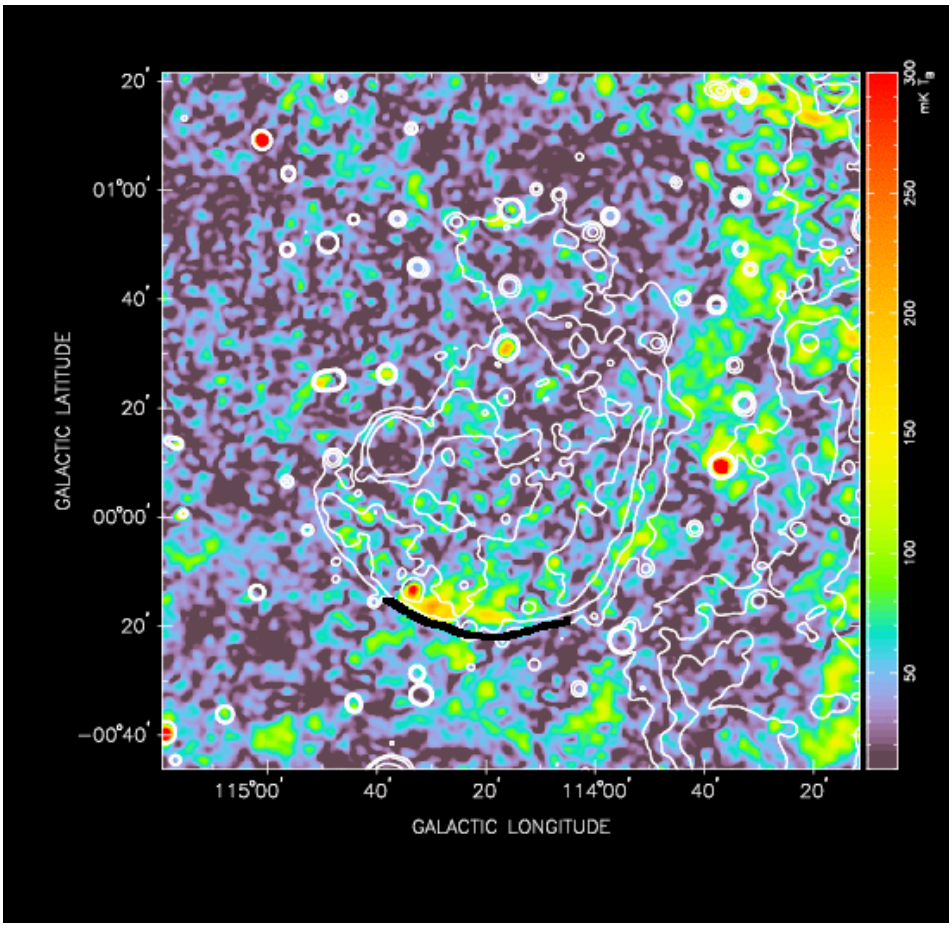

Fig. 5. Polarized intensity image of G114.3+0.3 as observed with the DRAO Synthesis Telescope. The optical filament towards the south of the SNR, observed by Mavromatakis et al. (2002), is marked in black.

References

Fesen R.A., Winkler P.F., Rathore Y. et al. (1997) *Astron. J.* **113**, 767.
Fürst E., Reich W. & Seiradakis J.H. (1993) *Astron. Astrophys.* **276**, 470.
Kulkarni S.R., Predehl P.R., Hasinger G. et al. (1993) *Nature* **362**, 135.
Landecker T.L., Dewdney P.E., Burgess T.A. et al. (2000) *Astron. Astrophys. Suppl.* **113**, 767.
Mavromatakis F., Boumis P. & Paleologou E.V. (2002) *Astron. Astrophys.* **383**, 1011.
Mitra D., Wielebinski R., Kramer M. & Jessner A. (2003) *Astron. Astrophys.* **398**, 303.
Reich W. & Braunsfurth E. (1981) *Astron. Astrophys.* **99**, 71.
Reich P., Reich W. & Fürst E. (1997) *Astron. Astrophys. Suppl.* **126**, 413.
Taylor A.R., Gibson S.J., Peracaula M. et al. (2003) *Astron. J.* **125**, 3145.
Taylor J.H. & Cordes J.M. (1983) *Astrophys. J.* **411**, 674.
Uyanıker B., Landecker T.L., Gray A.D. & Kothes R. (2003) *Astrophys. J.* **585**, 785.
Yar-Uyanıker A., Uyanıker B. & Kothes R. (2004) *Astrophys. J.*, in press.

"The Magnetized Interstellar Medium"
8–12 September 2003, Antalya, Turkey
Eds.: B. Uyanıker, W. Reich & R. Wielebinski

The Cygnus Loop: Two Colliding Supernova Remnants*

B. Uyanıker[1,2], W. Reich[1], A. Yar-Uyanıker[1,2], R. Kothes[2,3], and E. Fürst[1]

[1] Max-Planck-Institut für Radioastronomie, Auf dem Hügel 69, 53121 Bonn, Germany
[2] National Research Council, Herzberg Institute of Astrophysics, Dominion Radio Astrophysical Observatory, P.O. Box 248, Penticton, B.C., V2A 6J9 Canada
[3] Department of Physics and Astronomy, The University of Calgary, 2500 University Dr. NW, Calgary, AB, T2N 1N4 Canada

Abstract. The Cygnus Loop was often classified as a middle-aged supernova remnant (SNR) located below the Galactic equator ($\ell = 74^\circ, b = -8\overset{\circ}{.}6$) at a distance of 770 pc. Its large size and little confusion with Galactic emission makes it an ideal test ground for evolutionary and structural theories of SNRs. Here we present radio images of the Cygnus Loop at 2675 MHz, including polarization, together with an X-ray map at 0.25 keV. Radio continuum and polarization data provide indications that the Cygnus Loop consists of two separate SNRs. Combining this result with data from the literature we argue that a secondary SNR exists in the south with a recently detected neutron star close to its center. Two interacting SNRs seem to be the best explanation to account for the Cygnus Loop observations at all wavelengths.

1 Introduction

The Cygnus Loop, a question mark shaped supernova remnant (SNR) close to the Galactic plane ($\ell = 74^\circ$, $b = -8\overset{\circ}{.}6$), reckoned to be the representative of middle-aged SNRs, is the topic of this contribution. This SNR is close to us (∼770 pc, Minkowski (1958) or ∼ 440 pc according to Blair et al. (1999)) and by being relatively unaffected by the complex Cygnus region provides most detailed information on middle-aged SNRs. Therefore, the Cygnus Loop is generally considered as the test bed of SNR studies at almost all available wavelengths, including X-ray, optical, infrared and radio.

Here we present radio polarization images of the Cygnus Loop, together with the ROSAT 0.25 keV image, which were used in a previous study asserting that the Cygnus Loop in fact consists of two separate but interacting SNRs (Uyanıker et al. 2002). The analysis of these data together with available information on the rotation measure (RM), X-ray, optical, and infrared observations of the Cygnus Loop are used to constrain the characteristics and the relation of both SNRs.

2 Radio maps

Recently, sensitive radio maps of the Cygnus Loop at 2675 MHz obtained with the Effelsberg 100-m telescope with an angular resolution of $4\overset{\prime}{.}3$ were presented by Uyanıker et al. (2002). These maps of total intensity and polarization are shown in Fig. 1.

Clearly, the shape of the Cygnus Loop is circular in the north, while its southern extension resembles a crescent whose western part is incomplete and confuses with weak peripheral emission. Nevertheless, the southern crescent is brighter than most of the northern part of the Cygnus Loop. Total intensity differences and spectral index variations of $\Delta\alpha \sim 0.2$ led Green (1990) to conclude that the northern part of the remnant is governed by a compressed magnetic field and that the southern part results from shock acceleration. Morphologically the northern total intensity emission supports the idea that the SN shock compresses and deforms the ambient Galactic magnetic field and thus traces the local magnetic field (Green 1984). The partial shells in the north are aligned along the direction of the magnetic field as indicated in Fig. 2.

*Based on observations with the Effelsberg 100-m telescope operated by the Max-Planck-Institut für Radioastronomie (MPIfR), Bonn, Germany

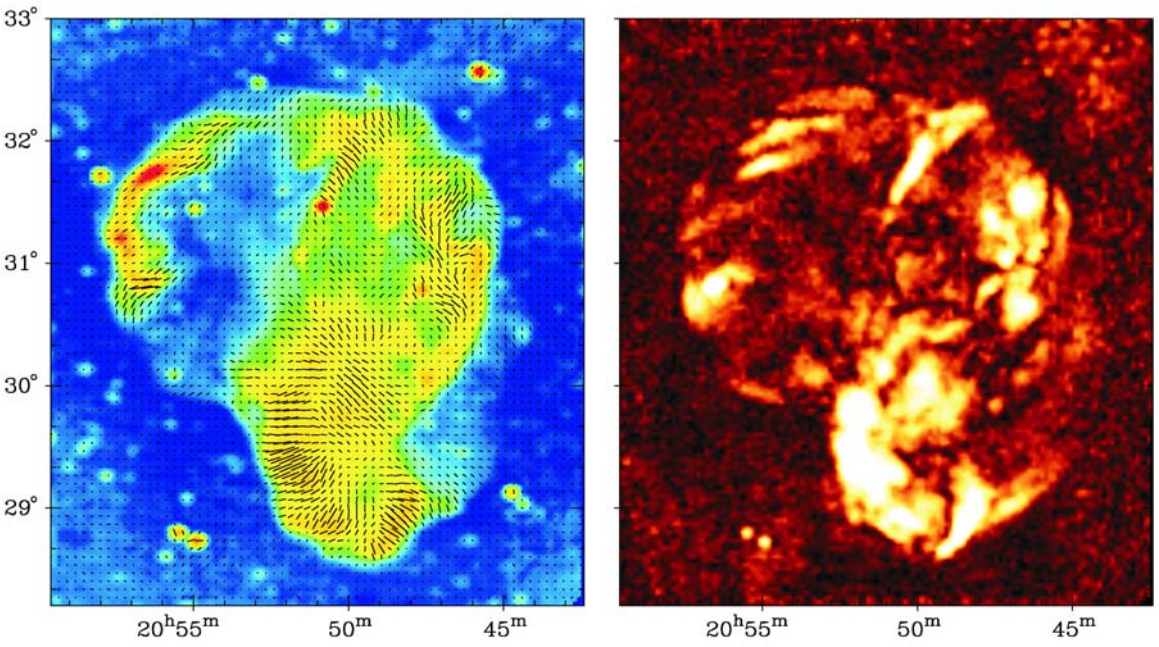

Fig. 1. Radio images of the Cygnus Loop at 2675 MHz at a resolution of 4.′3 as observed by Uyanıker et al. (2002) with the Effelsberg 100-m telescope. Both images are in the rectangular RA/Dec coordinate system (J2000). The total intensity map is shown (left panel), where color coding represents continuous intensity levels from 0 mK T_B (blue) to 500 mK T_B (red). The overlaid bars are electric field vectors proportional to the polarized intensity. The polarized intensity image of the same region is displayed on the right hand panel. Here the color coding represents levels from 0 mK T_B (red) to 90 mK T_B (white).

The total intensity and polarization images as displayed in Fig. 1 also show a diffuse radio plateau enveloping the conventional bright radio appearance of the remnant. This plateau was not visible in previously published radio maps and is the counterpart of similar emission seen at X-rays and in the infrared. With that feature we note a general agreement in the radio, X-ray and infrared appearance for the northern shell of the Cygnus Loop.

The 2675 MHz polarization image (Fig. 1) shows strong polarization towards the south (up to 30%) and for the prominent filament almost dividing the northern shell into two symmetrical half shells. Outside that filament the percentage polarization in the northern part is much lower than in the south. RM calculations from the reprocessed four bands of the 1420 MHz DRAO archival interferometric maps (previously published by Leahy et al. 1997) together with the presented 2675 MHz data, as well as a previous analysis by Kundu & Becker (1972), suggest that RMs vary across the remnant from -10 to -36 rad/m^2, with a mean of about -20 rad/m^2. Such a RM will rotate the observed polarization angle at 2675 MHz by about 15°, and therefore the 2675 MHz polarization vectors closely trace the orientation of the magnetic field.

The asymmetric polarization distribution between the southern and the northern part seems to be intrinsic. The polarized intensity in the southern part delineates a second circular shell corresponding to the previously called "break-out" region with the magnetic field vectors aligned tangentially. The northern part displays a more complicated polarization appearance. The upper part of the polarized southern shell overlaps with the northern shell. This contradicts the previous interpretation that a shock from the northern area breaks out into the south. Tenorio-Tagle et al. (1985) proposed that the northern shell is the breakout of a SNR in the south. However, this scenario cannot explain the high X-ray emission from the northern shell and this model needs ambient material of higher density in the south, which is not indicated by observations in the infrared (Arendt et al. 1992), in H I (DeNoyer

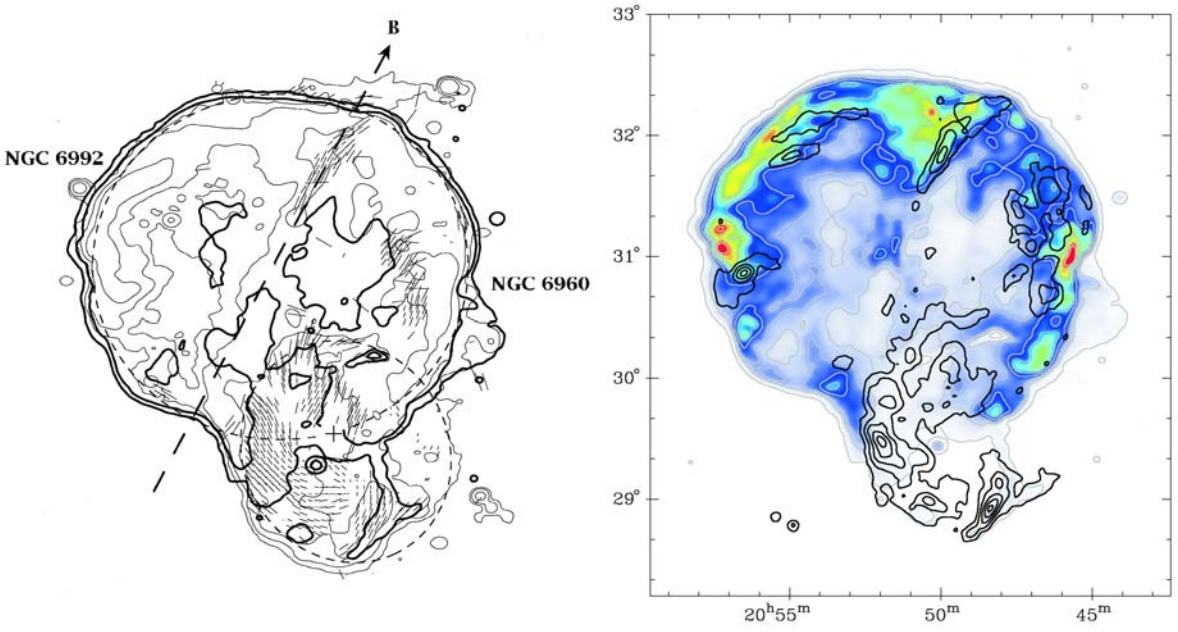

Fig. 2. Left panel: Sketch of the Cygnus Loop showing radio emission (thin lines) and 0.25 keV X-ray emission from ROSAT data (thick lines, convolved with a Gaussian beam of 3′). The positions and extents of the two SNRs are represented by dashed ellipses. The magnetic field vectors, obtained by using the polarization image given in Fig. 1 and corrected for Faraday rotation, are overlaid as bars. Pixels with low signal-to-noise ratio were omitted. The lengths of the vectors are proportional to RM. The direction of the large-scale magnetic field in this area of the Milky Way is shown by a dashed straight line, which passes through the polarized central filament in the north. The neutron star in the southern part is indicated by a plus sign. The two prominent optical filaments, NGC 6992 and NGC 6960, are labeled. Right panel: X-ray emission from the Cygnus Loop at 0.25 keV convolved with a 3′ beam. The X-ray intensities range from 0.002 counts s^{-1} $arcmin^{-2}$ to 0.25 counts s^{-1} $arcmin^{-2}$. Overlaid thick contours represent polarized intensity levels starting at 40 mK T_B running in steps of 40 mK T_B.

1975) and in CO (Scoville et al. 1977). A way out is to explain the Cygnus Loop by two separate remnants rather than by a single SNR.

The presence of the anomalous X-ray source AX J2049.6+2939 detected by the ASCA satellite (Miyata et al. 2001) at the center of the southern shell gives a strong hint that this part is a SNR independent from the large northern shell. Although no pulsed X-ray or radio emission was yet detected from this object, Miyata et al. (2001) conclude that this object is a stellar remnant, probably a neutron star.

3 Optical, X-ray and infrared data

The case that the Cygnus Loop consists of two SNRs is supported by optical, X-ray and infrared observations. Optical images (Levenson et al. 1998) reveal differences between the northern and the southern part of the Cygnus Loop. For example, Hα and O III regions are more extended in the north than in the south as a consequence of differences in the interaction with the surrounding gas.

The X-ray (Ku et al. 1984, Levenson et al. 1998) and infrared emission (Braun & Strom 1986) of the northern part is consistent with a limb-brightened shell of hot gas. The southern shell is almost invisible. This difference was taken as a sign for different mechanisms acting in the north and the south of the Cygnus Loop (Green 1990).

We conclude that observations at all wavelengths indicate different emission characteristics in the northern part compared to the southern region. A three-color composite image illustrating this

difference is displayed in Fig. 3. This image consists of three images: soft X-ray emission, total intensity and polarized intensity at 2675 MHz. Clearly, the northern part is dominated by the X-ray emission, whereas towards the south a distinct structure shows up. This southern part is dominated by radio emission.

Aschenbach & Leahy (1999) have interpreted the southern part of the remnant as a breakout into a lower density medium based on the smooth change of the X-ray emission from the northern towards the southern area. However, a smooth transition may also result from two SNRs seen in superposition. In Fig. 2 (right panel) we display the ROSAT soft X-ray image with overlaid polarization intensity contours showing minimum X-ray but maximum polarized emission in the area of overlap of the southern and northern shell. There are two regions ($\sim \alpha, \delta = 20^{\rm h}54^{\rm m}, 30^\circ$ to $\sim \alpha, \delta = 20^{\rm h}53^{\rm m}, 29^\circ 30'$) at the eastern and ($\sim \alpha, \delta = 20^{\rm h}48^{\rm m}, 29^\circ 45'$) at the western side, where X-rays are enhanced and also the peripheries of both shells superimpose. These observations suggest that both SNRs are not just seen in superposition, but are in physical interaction. Enhanced soft X-rays might emerge from the deceleration of the shock waves due to the collision of the SNRs. However, it is difficult to understand the minimum X-ray emission in the overlapping region. We like to mention that in the study of Williams et al. (1997), who observed the colliding SNRs DEM L316 in the Large Magellanic Cloud, also no X-ray emission was seen in the region of interaction. Details of the emission processes in the interacting regions need more theoretical investigation.

In the interaction scenario the SNR in the north exploded first and created a shell-type SNR. A second SN event took place at the position of AX J2049.6+2939. Shortly after the second explosion the shock waves of the SNRs collided and the younger southern SNR with a higher energy density swept up the shell of the northern remnant and bent it inward. The pronounced upper polarized shell of the southern SNR may be formed that way. The collision of the two shells also created the X-ray extensions encompassing the polarized emission (see Fig. 2). An estimate of the ages of the two SNRs by simply comparing their sizes, however, seems difficult since at least the northern remnant is suspected to be expanding in a pre-existing cavity (Charles et al. 1985, Levenson et al. 1997).

4 Discussion

Radio continuum measurements of the Cygnus Loop including linear polarization show differences between its southern and northern part. These differences are rather obvious by inspecting the polarized intensity image at 2675 MHz.

The following reasons led us to conclude that two SNRs make up the Cygnus Loop and are in interaction: First of all, the radio morphology of the Cygnus Loop differs in the south and in the north. Secondly, the distribution of polarized intensity differs completely in the south and in the north. It is shown that there is an intrinsic difference in the magnetic field configuration. Furthermore, a tangential magnetic field structure indicates a regular magnetic field configuration in the southern part being disturbed in the region of overlap. The magnetic field seems to be less regular in the north. In addition to that, previous radio spectral index work indicates a small change across the Cygnus Loop with a steeper spectrum in the south. The northern part has different characteristics of the optical filaments when compared to those in the southern region. The X-ray and infrared data indicate weak or no emission in the south in contrast to the strong radio emission. The X-ray enhancements at the superposition of the periphery of both shells indicate an interaction of both SNRs. Finally, there is evidence for the existence of a stellar remnant, probably a neutron star, almost exactly at the center of the southern shell.

The northern SNR G74.3−8.4 is centered at $\sim (\alpha, \delta) = (20^{\rm h}\ 51\overset{\rm m}{.}36,\ 31^\circ\ 3')$ with an extent of about $3\overset{\circ}{.}0 \times 2\overset{\circ}{.}6$. The southern remnant G72.9−9.0, whose extent is about $1\overset{\circ}{.}4 \times 1\overset{\circ}{.}8$, is centered at $\sim (\alpha, \delta) = (20^{\rm h}\ 49\overset{\rm m}{.}56,\ 29^\circ\ 33')$.

Acknowledgments

We like to thank Nancy Levenson for providing the 0.25 keV ROSAT mosaic used in Figs. 2 and 3.

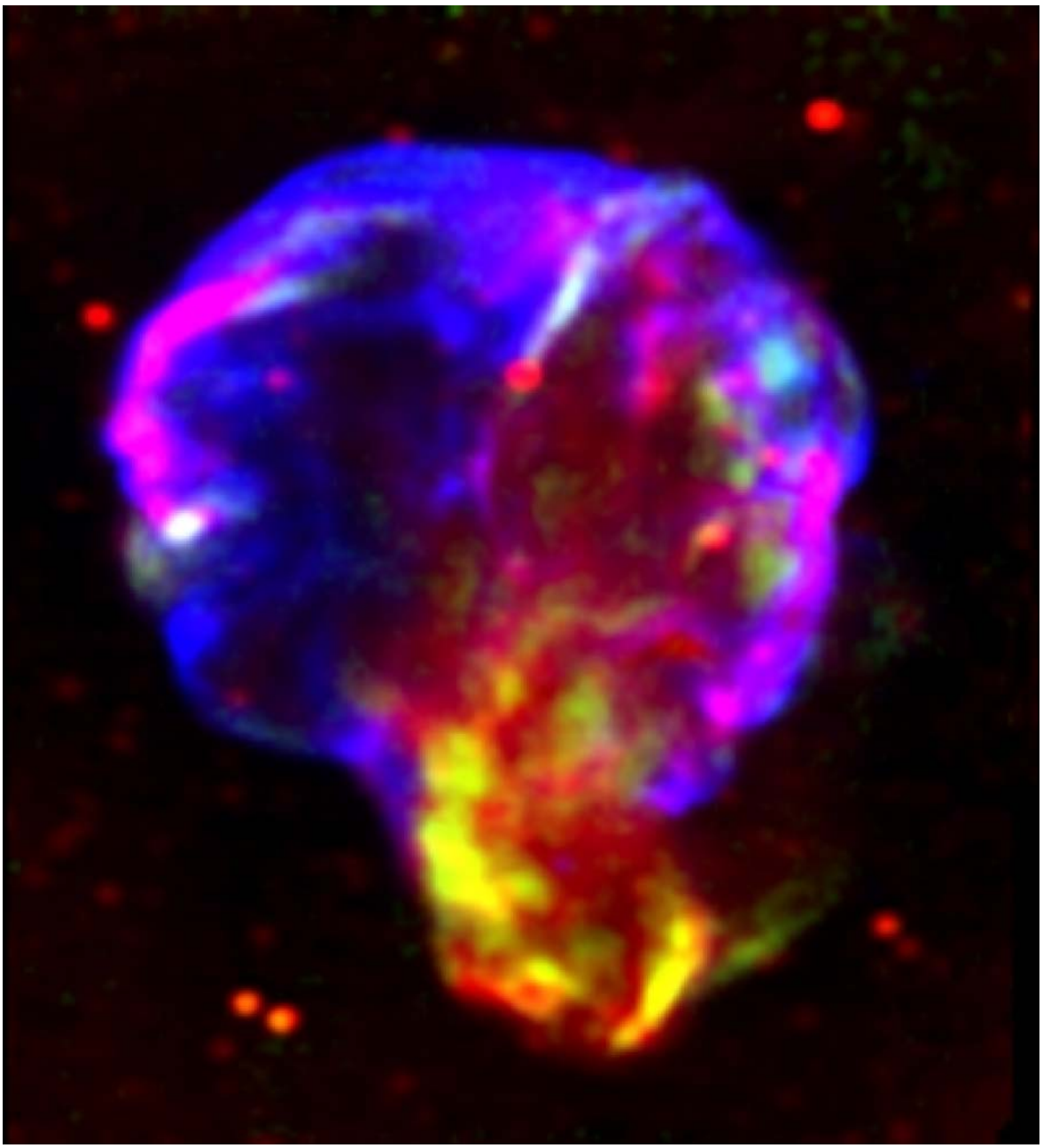

Fig. 3. Three-color composite image of the Cygnus Loop consisting of X-ray data from the ROSAT satellite, total intensity and polarized intensity images at 2675 MHz as observed with the Effelsberg 100-m telescope. The blue region dominating the northern part of the Cygnus Loop shows the X-ray emission. Red denotes regions where total intensity emission (e.g. NGC 6960 and NGC 6962) is observed. Polarized emission is shown by green, as prominently seen towards the southern part of the Cygnus Loop.

References

Aschenbach B., Leahy D. A. (1999) *Astron. Astrophys.* **341**, 602.
Arendt R. G., Dwek E., Leisawitz D. (1992) *Astrophys. J.* **400**, 562.
Blair W. P., Sankrit R., Raymond J. C., Long K. S. (1999) *Astron. J.* **118**, 942.
Braun R., Strom R. G. (1986) *Astron. Astrophys. Suppl.* **63**, 345.
Charles P. A., Kahn S. M, McKee C. F. (1985) *Astrophys. J.* **295**, 456.
DeNoyer L. K. (1975) *Astrophys. J.* **196**, 479.
Green D. A. (1984) *Mon. Not. R. Astron. Soc.* **211**, 433.
Green D. A. (1990) *Astron. J.* **100**, 1927.
Ku W. H.-M., Kahn S. M., Pisarski R., Long K. S. (1984) *Astrophys. J.* **278**, 615.
Kundu M. R, Becker R. H. (1972) *Astron. J.* **77**, 459.
Leahy D. A., Roger R. S., Ballantyne D. (1997) *Astron. J.* **114**, 2081.
Levenson N. A, Graham J. R., Aschenbach B., Blair W. P., Brinkmann W., Busser J.-U., Egger R., Fesen R. A., Hester J. J, Kahn S. M., Klein R. I., McKee C. F., Petre R., Pisarski R., Raymond J. C., Snowden S. L. (1997) *Astrophys. J.* **484**, 304.
Levenson N. A, Graham J. R., Keller L. D., Richter M. J. (1998) *Astrophys. J. Suppl.* **118**, 541.
Minkowski R. (1958) *Rev. Mod. Phys.* **30**, 1048.
Miyata E., Ohta K., Torii K., Takeshima T., Tsunemi H., Hasegawa T., Hashimoto Y. (2001) *Astrophys. J.* **550**, 1023.
Scoville N. Z., Irvine W. M., Wannier P. G., Predmore, C. R. (1977) *Astrophys. J.* **216**, 320.
Tenorio-Tagle G., Rozyczka M., Yorke H. W. (1985) *Astron. Astrophys.* **148**, 52.
Uyanıker B., Reich W., Yar A., Kothes R., Fürst E. (2002) *Astron. Astrophys.* **389**, L61.
Williams R. M., Chu Y.-H., Dickel J. R., Beyer R., Petre R., Smith R. C., Milne D. K. (1997) *Astrophys. J.* **480**, 618.

"The Magnetized Interstellar Medium"
8–12 September 2003, Antalya, Turkey
Eds.: B. Uyanıker, W. Reich & R. Wielebinski

Galactic Distribution and the Luminosity Function of Pulsars

I. Yusifov and İ. Küçük

Department of Astronomy & Space Sciences, Faculty of Arts & Sciences,
Erciyes University, Talas Yolu, 38039 Kayseri, Turkey

Abstract. We have studied the radial distribution and luminosity function of normal pulsars in the Galaxy, on the basis of the ATNF Pulsar Catalogue where the distances are calculated according to the new electron density model NE2001.
We show that the maximum of galactocentric distribution of pulsars located near 3.5 kpc and the scale-length of this distribution is ~ 4 kpc. The surface density of pulsars near the Galactic center (GC) is equal or slightly higher than that in the solar neighborhood. The local density and birth-rate of pulsars is 1.5 and 4 times higher than previous estimates, correspondingly before and after beaming corrections. The dependence of these results on the NE2001 model and recommendations for further improvement of the electron density distribution are discussed.
We derived the luminosity function of pulsars at frequencies near 1400 MHz. In the limited band of luminosities, the luminosity function has a slope near -1, but a new luminosity function may be better fitted by a Log–Normal distribution.

1 Introduction

The high-frequency, sensitive Parkes Multibeam Pulsar Survey (PMPS) (Manchester et al. 2001; Morris et al. 2002; Kramer et al. 2003) revealed many more distant pulsars with high Dispersion Measures (DM). These data may allow us to investigate in more detail the statistical parameters and distribution of pulsars, especially in the central regions of the Galaxy, which was almost impossible in previous low-frequency and less-sensitive surveys. Furthermore, high-frequency searches reveal many pulsars at the lower as well as at the high luminosity ends of the luminosity function (LF) of pulsars. From the evolutionary point of view it is of great interest for the influence of such pulsars on the shape of pulsars' LF.

Considering the actuality of the problem and with the appearance of publications with completely wrong interpretation of observational data of pulsars (Guseinov et al. 2002a, 2002b), we decided to estimate the density of pulsars at the GC and to take a fresh look at the radial distribution and luminosity function of pulsars using these new PMPS data, with the kind permission of Prof. R.N. Manchester, from the ATNF Pulsar Catalogue of 1412 pulsars (Manchester et al. 2002). We estimated the distances to the pulsars by using the NE2001 Galactic electron density model (Cordes & Lazio 2002, CL2002 hereafter).

In the space and luminosity distribution studies, it is very important to make corrections for the observational selection effects. In this contribution we used an empirical (and simple) method for the correction of observational selection effects, as in Kodiara (1974), Yusifov (1981), Leahy & Wu (1989), Wu & Leahy (1989, WL89 hereafter), with some modifications.

2 Available Data and the Selection Effects

At the time of preparing this contribution, the number of existing pulsars was 1412. The ATNF Pulsar Catalogue contains the data of PMPS, the Swinburne survey (Edwards et al. 2001) and all previous pulsar survey results, and it supplies a good sample of data for the statistical study of pulsars. Nearly 600 of them were discovered in the Parkes and Swinburne Multibeam Pulsar Surveys (MBPS).

In this study we are interested mainly in statistics of "normal" pulsars. For this reason we excluded from our sample binary and recycled ($\dot{P} < 10^{-17}$ s/s), globular cluster and extragalactic pulsars. In our study we mainly used pulsars in the regions of the Galactic latitudes $|b| \leq 15^{\circ}$ and longitudes

$-100° \leq l \leq 50°$. In this study, as in the Galactic electron distribution model NE2001, we used the IAU recommended value $R_{\odot} = 8.5$ kpc as the distance Sun–GC.

The apparent distribution of pulsars for the subsequent corrections due to selection effects is derived in the following manner. We drew equidistant concentric circles around the Sun (r_i) and the GC (R_j) and made up a quasi-regular grid of points at the points of intersection of these circles on the Galactic plane. Then we drew circles of radius R_{ci} around the grid points (or cells), counted the number of pulsars within the boundaries of circle R_{ci}, and estimated surface densities of pulsars around grid points. R_{ci} increasing linearly is chosen from $0.1R_{\odot}$ to 1/10 of the largest considered distances from the Sun (18.7 kpc) and calculated by the relation $R_{ci} = 0.85 * (1.2 * (i-1)/11 + 1)$, where i varies from 1 to 12. Similar variation of cell radii naturally reduces the density estimation errors at large distances due to distance uncertainties of pulsars.

Making corrections for the selection effects, we used these data for the calculation of the radial distribution of pulsars in the Galaxy. Selection effects we divide into two categories and define them by the relation:

$$\rho(r, R, l(r, R)) = K(l)K(r)\rho_o(r, R, l(r, R)) \ , \tag{1}$$

where l is the Galactic longitude; r and R distances from the Sun and the GC; $K(l)$ direction and $K(r)$ distance-dependent selection factors; $\rho_o(r, R, l(r, R))$ is the true and $\rho(r, R, l(r, R))$ is the observed distribution of surface densities of pulsars on the Galactic plane.

$K(l)$ is connected with the background radiation which leads to variations of the survey sensitivity with Galactic longitudes. Neglecting latitude dependence as in WL89, the direction-dependent correcting factor $K_1(l)$ is defined by the relation:

$$K_1(l) = 1 + \frac{T_{\mathrm{sky}\,1374}(l, b)}{T_{\mathrm{R}}} \ , \tag{2}$$

where $T_{\mathrm{sky}\,1374}(l, b)$ is the sky background temperature at 1374 MHz and $T_{\mathrm{R}} = 21$ K is the noise temperature of the Parkes multibeam receiver (Manchester et al. 2001). The correction factor $K_1(l)$ which was calculated from Eq. (2) is shown in Fig. 1. The observational number (or density) must be corrected for this selection effect, multiplying by $K_1(l)$. It is evident that $K(l)$ in Eq. (1) is equal to $K_1^{-1}(l)$. In the anticenter direction and in the cell where the Sun is located, $K_1(l)$ is assumed to be 1.

The distance-dependent selection factor $K(r)$ in Eq. (1) is the function of pulse broadening caused by scattering, scintillation etc. Here we make the simplifying assumption that the combined effect of these factors may be described by the exponential law as:

$$K(r) = K_1(r)K_2(r)\cdots K_i(r) = e^{-c_1 r}e^{-c_2 r}\cdots e^{-c_i r} = e^{-cr} \ , \tag{3}$$

where $K_1(r)$, $K_2(r)$ etc. are the distance-dependent correction factors relating to the pulse broadening, scattering and other selection effects. The quantitative estimation of each of these factors indepen-

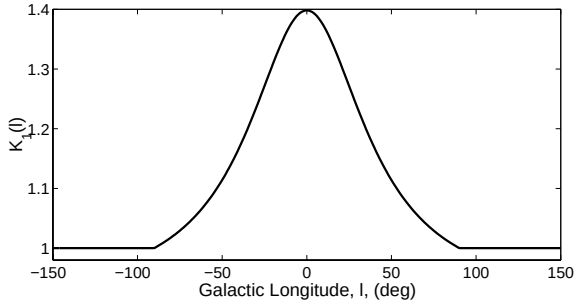

Fig. 1. Dependence of the correcting factor $K_1(l)$ as a function of Galactic longitude.

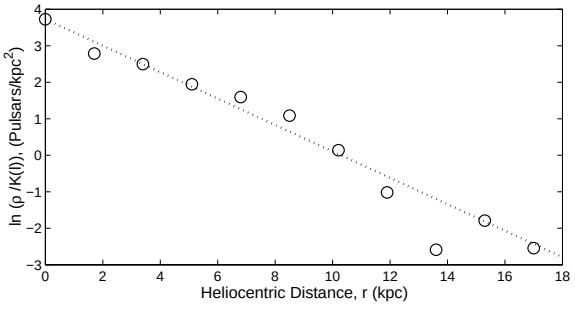

Fig. 2. Variation of the surface densities of pulsars on the galactocentric circle $R_{\odot} = 8.5$ kpc at various distances from the Sun.

dently is difficult. But the combined effect of these factors leading to reduced detection of pulsars away from the Sun may be estimated empirically as described below.

Assuming that the surface density of pulsars is symmetric around the GC, and considering a galactocentric circle with the radius $R_\odot$, from Eq. (1) we obtain:

$$\rho(r, R_\odot) = K(l)K(r)\rho_o(r, R_\odot) \ . \tag{4}$$

where $\rho(r, R_\odot)$ is the observable density; $K(l)$ is known and $\rho_o(r, R_\odot)$ is constant.

In order to derive $K(r)$ from Eq. (4), in Fig. 2, we have plotted $\rho(r, R_\odot)/K(l)$ against the heliocentric distance by circles.

Fitting the data in Fig. 2 by the least mean-squares (LMS) method for the distance-dependent correction factor we obtain:

$$K(r) = \exp(-cr) \ , \tag{5}$$

where $c = 0.362 \pm 0.017$ and $ln\rho_o = 3.73 \pm 0.16$.

3 Radial Distribution and the Luminosity Function of Pulsars

The true densities of pulsars were found from the apparent densities, after correcting them by the relation (1). $K(l)$ and $K(r)$ are calculated from Eqs. (2) and (5) respectively. The radial distributions of densities from the GC may be found by averaging the densities $\rho(r, R)$ at various distances (R_j) from the GC.

The results of obtained radial distribution of surface densities of pulsars (squares) with corresponding error bars, together with the distribution of other Population I objects, are plotted in Fig. 3. In evaluating errors, we assumed that the number of pulsars in cells, in a rough approximation, follows the Poisson statistics. The errors for various data points are not equal, so we calculated the weighted average of surface densities and corresponding errors. In order to simplify the comparison with other results, the densities in Fig. 3 are normalized to the surface densities at the solar circle.

Within the galactocentric radius 0.5 kpc pulsars are absent; and from the available data and precision of distance estimates, it is difficult to estimate the density of pulsars there. But within the range 0.5 kpc < R < 1 kpc there are 4 pulsars. Applying the correction factors $K(l)$ and $K(r)$ to the apparent density, we obtain 50 pulsars kpc^{-2}. In fitting the radial distributions of pulsars, just this value will be used.

The radial distribution of pulsar surface densities in Fig. 3 has been fitted by the relation:

$$\rho(R) = A\left(\frac{R}{R_\odot}\right)^a \exp\left[-b\left(\frac{R - R_\odot}{R_\odot}\right)\right] \ , \tag{6}$$

where $R_\odot = 8.5$ kpc is the Sun−GC distance. The best results of the fits are: $A = 37.8 \pm 2.1$ kpc^{-2}, $a = 1.12 \pm 0.10$ and $b = 3.20 \pm 0.24$.

Revising Fig. 3, it is seen that high frequency, high sensitive PMPS searches revealed many pulsars around the GC, and within error limits the derived density (50±16 pulsars kpc^{-2}) is not less than that in the circumsolar region. Applying the Tauris & Manchester (1998, TM98 hereafter) beaming model, for this value we obtain (500±150) pulsars kpc^{-2}.

In Fig. 3 we compare radial distributions of pulsars and SNR with the radial distributions of their progenitors. It is seen that, although the maxima of Population I objects coincide, the maximum of pulsar distribution is shifted to the GC by nearly 1.5 kpc. The maxima of pulsar and SNR distributions nearly coincide. But the radial scale length (RSL) of pulsar distributions (~ 4 kpc) is nearly two times less than the SNR distributions.

In Fig. 3 we also plotted by dots the radial distribution of the birth location of NS which was derived by Paczynski (1990). Although the maximum of this distribution coincides with the maximum of the SNR distribution, its shape considerably deviates from the distribution of Population I objects. If the progenitors of NS are OB-type Population I stars, then from qualitative considerations of Fig. 3, it

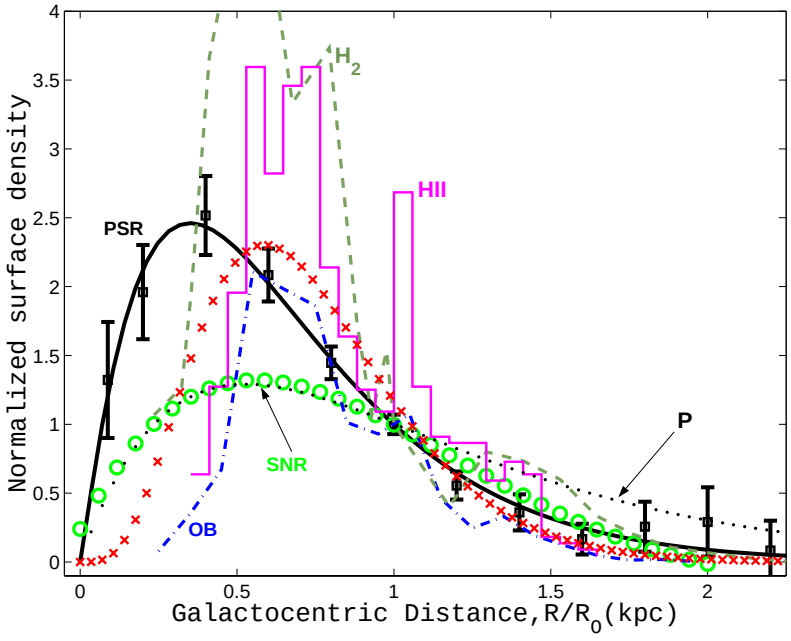

Fig. 3. Radial distributions of pulsars (squares) and other types of Population I objects: SNR distributions are from Case & Bhattacharya (1998); H2 column densities from Bronfman et al. (1988) and Wouterloot et al. (1990); H II regions are from Paladini et al. (2004) (it must be noted that H II regions represent the number of sources in the 0.5 kpc wide Galactocentric rings, but not surface densities); OB star-formation regions data from Bronfman et al. (2000); marked by **P** are the radial distributions of birth location of NS (from Paczynski 1990); the expected radial distributions of birth location of NS (Eq. (7)) are marked by crosses.

seems that the radial distribution of the birth location of NS must be located near the line shown by crosses in Fig. 3 and may be described by the relation:

$$\rho(R) = A\left(\frac{R}{R_\odot}\right)^a \exp\left[-b\left(\frac{R}{R_\odot}\right)\right], \tag{7}$$

where $a = 4$, $b = 6.8$ and $R_\odot = 8.5$ kpc is the Sun–GC distance. The constant A must be chosen from the calibration constraints (particularly, in the current case A = 1050).

In order to construct LF, we selected the sample of pulsars within a cylinder of radius 2 kpc from the Sun. For faint pulsars we applied standard volume correcting methods, and LF is calculated as

$$\Phi(L) = \Phi_O(L)\frac{V_{\max}}{V[< d(L)]}, \tag{8}$$

where $\Phi(L)$ is the true LF, $\Phi_O(L)$ is the apparent LF, $V[< d(L)]$ is the volume of sphere with radius $d(L)$ from the Sun in which pulsars with luminosities L are still observable, $V_{\max} = 2\pi d^2(L) z_{\max}$ is the volume of cylinder of radius $d(L)$ around the Sun and $z_{\max}$ is the approximate value of the maximum height of pulsars from the Galactic plane. We accept that $z_{\max} = 2$ kpc, and pulsars outside these altitudes are not more than 2–5% of observable pulsars.

The LF calculated on the basis of these data is presented in Fig. 4. The total number of observable pulsars in every luminosity bin is estimated on the basis of all available pulsars, but taking into account that high sensitive MBPS are carried out only in the region of $|b| \leq 15^\circ$ and $-100^\circ \leq l \leq 50^\circ$.

For the low-luminosity pulsars the LF is estimated from relation (8), where $z_{\max}$ is assumed to be 2 kpc. There are only two pulsars with luminosities > 100 mJy kpc^2 in the considered region of d < 2 kpc around the Sun. $\Phi(L)$ values for them are calculated on the basis of large-distance pulsars revealed in the MBPS, assuming that they are observable almost everywhere in the Galaxy.

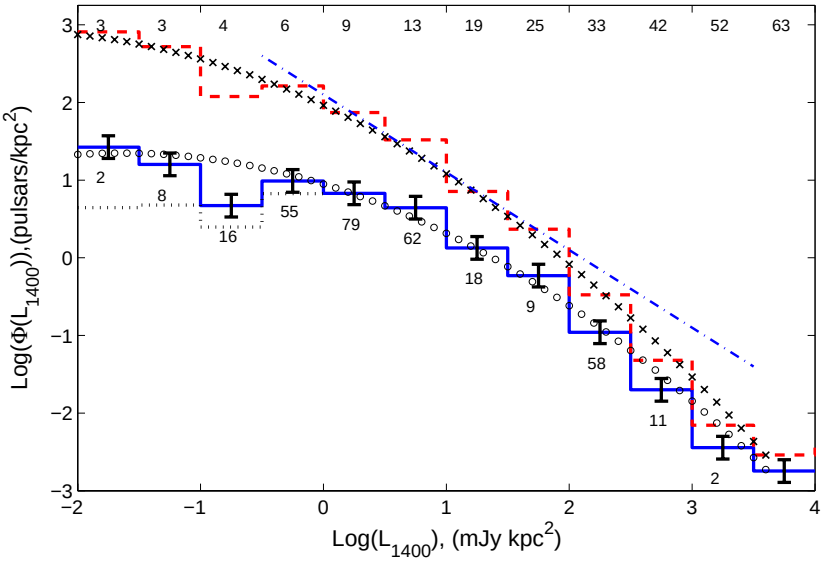

Fig. 4. Observed and corrected LF of pulsars. The observed number of pulsars in the luminosity bins are indicated under the corresponding bin. The observed distribution is given by the dotted line. A solid line shows the volume-corrected distribution of observable pulsars. The errors here represent the statistical uncertainty (30%) in distance estimates. A dashed line shows the distribution of active pulsars, after applying beaming correction. Lines marked by circles and crosses correspond to the Log–Normal fitting of observed and corrected data by the relation (9). A dash-dotted line corresponds to the fitting of the data above $\sim$1 mJy kpc^2 assuming a slope of -1.

In this study we applied the TM98 beaming model for the correction of LF. We estimated approximate values of the beaming fraction (BF) corresponding to each luminosity bin and show them at the top of Fig. 4 in percent. LF, corrected according to these BFs, is shown by the dashed line in Fig. 4.

The MBPS nearly doubled the number of pulsars around 0.1 mJy kpc^2, but it is not enough to describe the LF by one straight line. As is seen in Fig. 4, only the LF in limited regions of luminosities may be fitted by a straight line. A flattening of LF at low luminosities was already noted in previous studies and explained as a result of the deficit of low-luminosity stars (see Lyne et al. 1985; Guseinov & Yusifov 1986; Cordes & Chernoff 1997; Lyne et al. 1998, and references therein). We fitted the data in Fig. 4 by the Log–Normal distribution before and after beaming corrections by one analytical relation:

$$\Phi(L) = \frac{A_L}{\sigma_L\sqrt{2\pi}} \exp\left[-\frac{1}{2}\left(\frac{\log L - \log L_O}{\sigma_L}\right)^2\right] \text{ pulsars kpc}^{-2} \ . \tag{9}$$

For the constants of distributions A_L, σ_L and $\log L_O$ before and after beaming corrections, we obtained values 67$\pm$15; 1.21$\pm$0.07; $-$1.64$\pm$0.33 and 2600$\pm$600; 1.24$\pm$0.10; $-$2.60$\pm$0.57 correspondingly.

4 Results and Discussion

We have studied the population of normal pulsars in the Galaxy, using the ATNF Pulsar Catalogue where the distances are calculated according to the new electron densities model NE2001.

We have derived the radial distribution of surface density of normal pulsars by using the new distances. The maximum of radial distribution is located at $\sim$3.5 kpc and $\sim$1.5 kpc nearer to the GC relative to the maximum of distributions of Population I objects. Although the maximum of the distribution nearly coincides with the maximum of distributions of their progenitors (SNRs), the RSL of pulsars is $\sim$4 kpc, i.e. nearly two times less than the SNR distribution. Integrating the radial distribution for the total number of normal pulsars with luminosities $L_{1400} \geq 0.1$ mJy kpc^2 in the Galaxy, we obtained $(24 \pm 3) \times 10^3$ and $(240 \pm 30) \times 10^3$ before and after applying beaming corrections.

The surface density of pulsars around the GC region is (50±16) pulsars kpc^{-2} and (500±150) pulsars kpc^{-2} before and after applying beaming corrections.

For the luminosities at 1400 MHz, the LF of pulsars is constructed on the basis of pulsars within 2 kpc from the Sun. In estimating beaming corrections we applied pulsar beaming models of TM98. The low luminosity end flattening of LF became increasingly more evident. The LF of pulsars may be better described by the Log–Normal distribution (Eq. 9). Above a luminosity value of 0.1 mJy kpc^2 for the local surface density of normal pulsars we obtained (41 ± 5) pulsars kpc^{-2} and (520 ± 150) pulsars kpc^{-2} before and after beaming corrections. Assuming $\tau = 10^7$yr as the mean life time of active pulsars, for the corresponding birth-rate of pulsars in the solar neighborhood we obtain 4 and 52 pulsars kpc^{-2} Myr^{-1} respectively before and after beaming corrections.

We recommend a new relation (Eq. (7)) for the expected radial distribution of birth location of NSs, which is more closely related to the radial distribution of Population I objects.

The total number and frequency of generation normal pulsars obtained from these data are nearly 1.5 and 4 times higher than previous estimates, correspondingly before and after beaming corrections. One of the reasons for the higher values is possibly connected with the overestimated electron densities of the ISM. This leads to the necessity of further improvement of the Galactic electron density model, which requires H I measurements for distant pulsars.

One of the recent, but unsuccessful, attempts on pulsar distances and LF estimations are the publications of Guseinov et al. (2002a, 2002b). However, due to the fallacy of their method and approaches to the problem and other numerous errors, their results are not discussed here.

A more complete report on this work will be given elsewhere (Yusifov and Küçük, in preparation).

Acknowledgments

We would like to thank R.N. Manchester and the Parkes Multibeam Pulsar Survey team for making the parameters of new pulsars available on the internet prior to formal publication. We thank R. Wielebinski, J.L. Han and F.F. Özeren for reading the manuscript and for useful discussions. We thank Victor B. Cohen for help in preparing the manuscript. This work has been partially supported by Erciyes University R/D project No. 01−052−1, Turkey. Extensive use was made of both the Los Alamos preprint archive and the ADS system.

References

Bronfman, L., Cohen, R.S., Ajvarez, H., May, J., & Taddeus, P. (1988) *Astrophys. J.* **324**, 248.
Bronfman, L., Casassus, S., May, J., & Nyman, L.-Å (2000) *Astron. Astrophys.* **358**, 521.
Case, J.L. & Bhattacharya, D. (1998) *Astrophys. J.* **504**, 761.
Cordes, J.M. & Chernoff, D.F. (1997) *Astrophys. J.* **482**, 971.
Cordes, J.M. & Lazio, T.J.W. (2002) preprint [astro-ph/0207156].
Edwards, R.T., Bailes, M., van Straten, W., & Britton, M.C. (2001) *Astrophys. J.* **326**, 358.
Guseinov, O.H., Yazgan, E., Özkan, S., & Tagiyeva, S. (2002a) *Rev. Mex. Astron. Astrof.* **39**, 267.
Guseinov, O.H., Yazgan, E., Özkan, S., Tagiyeva, S., & Yoldas, A.K. (2002b) preprint [astro-ph/0207306].
Guseinov, O.H. & Yusifov, I.M. (1986) *Sov. Astron.* **30**, 47.
Kodiara, K. (1974) *Publ. Astron. Soc. Japan* **26**, 255.
Kramer, M., Bell, J.F., Manchester, R.N., et al. (2003) *Mon. Not. R. Astron. Soc.* **342**, 1299.
Leahy, D.A. & Wu, X. (1989) *Publ. Astron. Soc. Pac.* **101**, 607.
Lyne, A.G., Manchester, R.N. & Taylor, J.H. (1985) *Mon. Not. R. Astron. Soc.* **213**, 613.
Lyne, A.G. , Manchester, R.N., Lorimer, D.R., Bailes, M., D'Amico, N., Tauris, T.M., Johnston, S., Bell, J.F., & Nicastro, L. (1998) *Mon. Not. R. Astron. Soc.* **295**, 743.
Manchester, R.N., Lyne, A.G., Camilo, F., et al. (2001) *Mon. Not. R. Astron. Soc.* **328**, 17.
Manchester, R.N., et al. (2002) *ATNF Pulsar Catalogue*, http://www.atnf.csiro.au/research/pulsar/psrcat
Morris, D.J., Hobbs, G., Lyne, A.G., et al. (2002) *Mon. Not. R. Astron. Soc.* **335**, 275.
Paczynski, B. (1990) *Astrophys. J.* **348**, 485.
Paladini, R., Davies, R., & DeZotti, G. (2004) in *From Observations to Self-Consistent Modeling of the Interstellar Medium*, eds. M. Avillez & D. Breitschwerdt, *Astrophys. & Space Sci.*, in press [astro-ph/0212341].
Tauris, T.M. & Manchester, R.N. (1998) *Mon. Not. R. Astron. Soc.* **298**, 625.
Wouterloot, J.G.A., Brand, J., Burton, W.B. & Kwee, K.K. (1990) *Astron. Astrophys.* **230**, 21.
Wu, X. & Leahy, D.A. (1989) *Acta Ap. Sinica* **9**, 233.
Yusifov, I.M. (1981) *Former Soviet Astr. Circ.* **1164**, 1.

"The Magnetized Interstellar Medium"
8–12 September 2003, Antalya, Turkey
Eds.: B. Uyanıker, W. Reich & R. Wielebinski

Pulsars and the Warp of the Galaxy

I. Yusifov

Department of Astronomy & Space Sciences, Faculty of Arts & Sciences,
Erciyes University, Talas Yolu, 38039 Kayseri, Turkey

Abstract. This paper studies the asymmetries of pulsar distributions relative to the Galactic plane in various Galactic longitudes. It is shown that the observed asymmetric distribution may be explained by the warped and flaring (i.e. increase of scale-height at the peripheries of the Galaxy) structure of the Galaxy. At the peripheries of the Galaxy, the amplitude of the warp, derived from these data, may be as high as ∼1 kpc. The scale-height of the pulsar distribution increases exponentially from ∼0.5 kpc to ∼1 kpc while increasing the galactocentric distance from 5 kpc to 15 kpc. The warp and flare parameters derived from the pulsar data are compared with the stellar and gaseous warp and flare parameters of the Galaxy.

1 Introduction

The existence of a Galactic warp has been known since the first radio surveys of the Galaxy (Burton 1988). Furthermore, it was shown that the distribution of various Galactic components at the peripheries of the Galaxy also shows a flaring structure; i.e., growth of scale-height with increasing Galactic radius. Subsequently, the warped and flaring structure of the Galaxy was studied for young OB stars and old stellar components of the Galaxy, as well as for the Galactic dust emission at 240 μm (e.g. Alard 2000; Drimmel et al. 1999; Drimmel & Sperge 2001; López-Corredoira et al. 2002a).

The stability and the precise shape and nature of the Galactic warp, however, still remain unclear. The Large Magellanic Cloud, the Sagittarius dwarf galaxy and intergalactic accretion are considered as possible sources of generating Galactic warps (see for example García-Ruiz et al. 2002; Tsuchiya 2002; López-Corredoira et al. 2002b; and Bailin 2003).

It is generally accepted that the progenitors of pulsars are young OB stars, and if their Galactic distributions show warped structure (Drimmel et al. 1999), then the distribution of pulsars also must reveal a similar structure. As objects observable from large distances, pulsars may be more appropriate to study the warped and flaring structure of the Galaxy.

The recent high-frequency, sensitive Parkes Multibeam Pulsar Surveys (PMPS) (Manchester et al. 2001; Morris et al. 2002; and Kramer et al. 2003) revealed many more distant pulsars with high Dispersion Measures (DM). These and all other available observational data of pulsars are collected in new ATNF Pulsar Catalogue (Manchester et al. 2002). The warp and flare of the Galaxy may be estimated analyzing the longitude and latitude distribution of pulsars from this catalogue.

However, warp and flare are more pronounced at distances larger than 10 kpc from the Galactic center and from the Sun. Unfortunately, at present, the number of observable pulsars at these distances is rather small. Probably, more precise estimates of the warp and flare parameters may be possible when a greater number of pulsars will be detected at the peripheries of the Galaxy. However, preliminary studies of warp and flare may be done with the data already available, which is presented in this contribution. Furthermore, warped and flaring structures of the Galactic plane may be used in future to attain a more detailed modeling of the Galactic electron distribution and more precise estimates of distances for some distant pulsars.

2 Observed Data and Warped Disc Model of the Galaxy

Yusifov & Küçük (this volume, YK2003 hereafter) have studied the Galactic distribution and the luminosity function of pulsars on the basis of new ATNF catalogue of 1412 pulsars (Manchester et

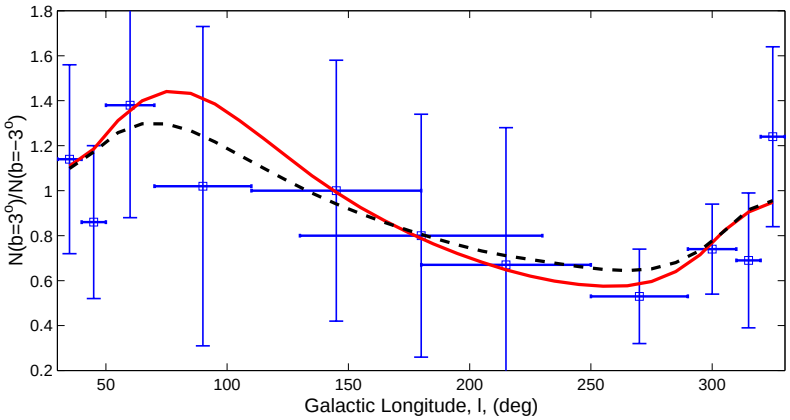

Fig. 1. Ratio of positive counts of pulsars to negative ones with corresponding errors. Horizontal bars correspond to the width of the considered longitude intervals. Dashed and solid lines correspond to the best-fitting models with and without taking into account data points at longitude $l = 90°$.

al. 2002). We have used here the results of this study to derive the warp and flare parameters of the Galaxy.

The estimates of the parameters of the warp and flare were made by the method described in López-Corredoira et al. (2002a), with some modifications. For this study we select "normal" pulsars at Galactic latitudes $|l| \leq 5°$, excluding binary and recycled ($\dot{P} < 10^{-17}$ s/s), globular cluster and extragalactic pulsars. We found the ratio of the cumulative number of pulsars above and below the Galactic plane at various Galactic longitudes centered at $b = \pm 3°$; the results with the corresponding error bars are plotted in Fig. 1. The errors in Fig. 1 are estimated assuming that the observed cumulative numbers follow the Poisson distribution. In order to see the warping effect clearly, pulsars located within $r \leq 1$ kpc from the Sun were excluded from consideration.

The number of pulsars at various longitudes varies dramatically, and in order to gather a statistically significant number of pulsars, as is seen from Fig. 1, the longitude width of the interval was chosen to be variable. The latitude width of the intervals, which is centered on $b = \pm 3°$, was $Deltab = 4°$.

In spite of the existence of large error bars, the plot clearly shows a sinusoidal behavior. If the warped structure were absent, the ratio of counts should be nearly the same for all Galactic longitudes. A similar behavior may be easily explained by the warp of the Galactic plane.

The parameters of the warp will be found from Fig. 1, fitting the observed ratios with the modeled ones. The stellar statistic equation has the form:

$$A(m) = \int_0^\infty r^2 D(r) \phi(M) dr \ , \tag{1}$$

where $A(m)$ is the number of stars per unit area of solid angle ω at m in interval dm, ϕ(M) is the luminosity function and $D(r)$ is the stellar density. Converting this relation to the pulsar data for our purpose, we obtain:

$$N(l,b) = \omega \int_{r_2}^{r_1} N_0(l,b,r) \rho[R(l,b,r), z(l,b,r)] r^2 dr \ , \tag{2}$$

where r and R are the distances from the Sun and the Galactic center, ρ is the space density and

$$N_0(l,b,r) = \int_{S_0 r^2}^{L_{\max}} \Phi(L) \frac{dL}{L} \tag{3}$$

is the local surface density of pulsars at distance r from the Sun. S_0 is the minimum detectable flux density, and $L_{\max} = 10^4$ mJy kpc^2 is the maximum luminosity of pulsars at 1400 MHz. For the

minimum detectable flux density we assume a derived value of $S_0 = 0.07$ mJy from YK2003. The Galactic distribution and luminosity function of pulsars accepted from YK2003 have the form:

$$\sigma(R) = C \left(\frac{R}{R_\odot}\right)^a \exp\left(-b\frac{R-R_\odot}{R_\odot}\right) , \tag{4}$$

where $\sigma(R)$ is the surface density of pulsars with parameters $C = 40$ kpc^{-2}, $a = 1.12$, $b = 3.2$, and $R_\odot = 8.5$ kpc is Sun–Galactic center distance and

$$\Phi(L) = \frac{A_L}{\sigma_L\sqrt{2\pi}} \exp\left[-\frac{1}{2}\left(\frac{\log L - \log L_O}{\sigma_L}\right)^2\right] , \tag{5}$$

where $A_L = 67, \sigma_L = 1.21$ and $\log L_O = -1.64$. The space distribution then has the form:

$$\rho(l,b,r) = N_0(l,b,r) \left(\frac{R}{R_\odot}\right)^a \exp\left(-b\frac{R-R_\odot}{R_\odot}\right) \exp\left(-\frac{|z|}{h_z(R)}\right) \frac{h_z(R)}{h_z(R_\odot)} , \tag{6}$$

where $h_z(R)$ is the scale-height of pulsar distributions. In order to study flaring of pulsar distributions in the model is included exponentially increasing scale-height by the relation:

$$h_z(R) = h_z(R_\odot) \exp\left(\frac{R-R_\odot}{h_{R,flare}}\right) , \tag{7}$$

where $h_z(R_\odot)$ and $h_{R,flare}$ are free parameters. The factor $\frac{h_z(R)}{h_z(R_\odot)}$ in Eq. (6) is normalized due to the variable scale-height of $h_z(R)$.

In order to take the warping structure into account in relation (6), $|z|$ must be replaced by $|z - Z_w|$, where the function $Z_w(R,\phi)$ describes the vertical displacement of the warp. From the early studies of H I it is known that the warping structure of the galaxy is asymmetric (see for example Burton (1988)), and at the galactocentric distances $R > 14$ kpc the southern warp becomes constant with height (see Fig. 2). For this reason, for the warped model of the Galactic plane, we include an additional free parameter, as the galactocentric radius R_{WS}, from which the southern warp becomes constant, and correspondingly $Z_w(R,\phi)$ is calculated by the relation:

$$Z_w(R,\phi) = \begin{cases} C_W(R-R_W)^{b_w}\sin(\phi-\phi_W)+15, & \text{for } R \le R_{WS} , \\ C_W(R_{WS}-R_W)^{b_w}\sin(\phi-\phi_W)+15, & \text{for } R > R_{WS} . \end{cases} \tag{8}$$

Here, R_W is the galactocentric radius, from which the warp starts (for $R < R_W$, $Z_w(R,\phi) = 0$), ϕ is the galactocentric angle taken in the direction of Galactic rotation with the Sun lying along $\phi = 0°$.

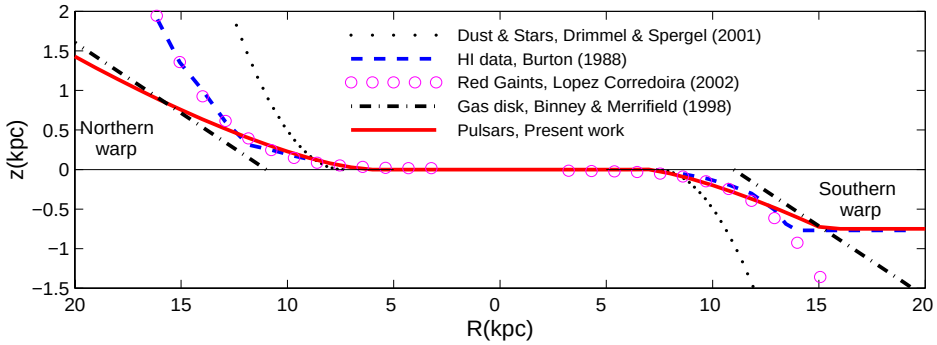

Fig. 2. Comparison of the maximum of amplitudes of the various Galactic warps models, plotted as a function of galactocentric distance. Data of all models were converted to $R_\odot = 8.5$ kpc.

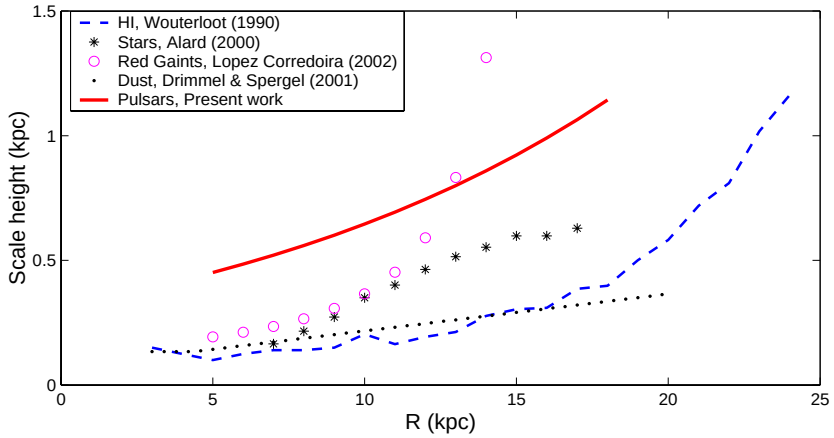

Fig. 3. Comparison of the scale-height variations of various Galactic components plotted as a function of distance to the Galactic center.

3 Results and Discussion

Using relations (2)–(8) we have fitted the observational data in Fig. 1 by the least mean square method and estimated the warp and flare parameters in Eqs. (7) and (8). For the best-fitting parameters we obtain:

$$h_z(R_\odot)=580 \text{ pc}, \quad h_{R,flare}=14 \text{ kpc}; \tag{9}$$

and

$$C_W=37, \quad R_W=6.5 \text{ kpc}, \quad b_w=1.4, \quad \phi_w=14.5^\circ \quad \text{and} \quad R_{WS}=15.2 \text{ kpc} \tag{10}$$

The results of fitting by these parameters are shown by the solid lines in Figs. 1–3. In Figs. 2 and 3 we compared the warp and flare results of our study with similar results of other studies. It is interesting to note that the warp of the galactic disc derived from pulsar data is more closely related to the gas disc warp (Binney & Merrifield 1998; Bailin 2003) than the stellar and dust warps, which are described in López-Corredoira (2002a) and Drimmel & Spergel (2001).

In fitting the observational data in Fig. 1, we used both a symmetric and asymmetric warp. Calculations show that the asymmetric warp better fits the observational data, and the obtained southern asymmetry is very closely related to H I data (see Fig. 2).

We estimated the scale-height of the pulsar distribution ($h_z(R_\odot) = 580$pc) here by quite a different method than that used (e.g. Lyne et al. (1985) and references therein) and it occurred nearly 30% greater than that of earlier estimates (450 pc). The large scale-height of pulsars may be caused by the additional fact of the high-velocity origin of pulsars.

From Fig. 3 it is seen that, as for other components of the Galaxy, the scale-height of the pulsar distribution also increased with increasing galactocentric radius. This increase strongly deviates from the red giant flaring and is nearly parallel to the H I and dust flaring.

From previous studies it was known that the line of nodes or phase angle of the warp (ϕ_w) is $\approx 0^\circ$ (see for example Drimmel & Spergel 2001) or even has a negative value $\approx -5^\circ$ (see for example López-Corredoira et al. 2002). But from fitting pulsar data in Fig. 1 we obtain $\phi_w \approx 15^\circ$ for the phase angle of the warp.

Figure 4 shows the general view of the Galactic plane obtained in this study. There are very few pulsars at distances $R > 15$ kpc, and for this reason the precise values of warping and flaring at these distances are still waiting to be elucidated. Nevertheless, this warping structure of the Galactic plane may be very helpful in distance estimates of some high-DM pulsars. The inclusion of the warping and flaring structure of the Galaxy to the large-scale modeling of the ISM electron distribution may serve as the next step to improve the model.

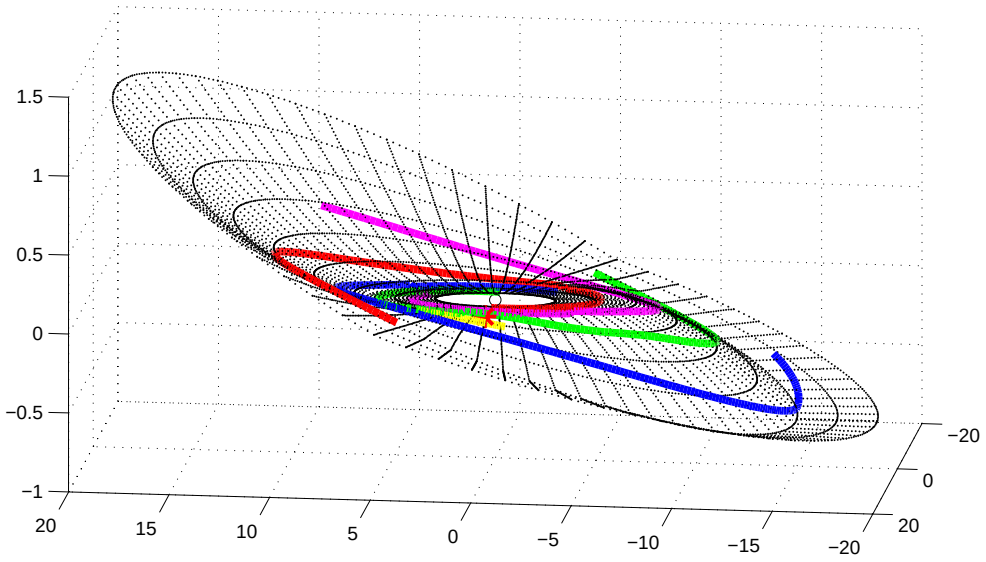

Fig. 4. A schematic 3D view of the Galactic warped plane together with spiral arms from Cordes & Lazio (2002). In order to present a better appearance of the warping structure, the scale in the z direction is considerably increased.

Acknowledgments

I would like to thank R.N. Manchester and the Parkes Multibeam Pulsar Survey team for making the parameters of new pulsars available on the internet prior to formal publication. I thank Victor B. Cohen for help in preparing the manuscript. This work has been partially supported by Erciyes University R/D project No. 01−052−1, Turkey. Extensive use was made of both the Los Alamos preprint archive and the ADS system.

References

Alard, C. (2000) preprint [astro-ph/0007013].
Bailin, J. (2003) *Astrophys. J.* **583**, L79.
Binney, J. & Merrifield, M. (1998) *Galactic Astronomy*, Princeton University Press.
Burton, W.B. (1988) in *Galactic and Extragalactic Radio Astronomy*, eds. K.I. Kellermann & G.L. Verschuur, Springer-Verlag, Berlin, p. 295.
Cordes, J.M. & Lazio, T.J.W. (2002) preprint [astro-ph/0207156].
Drimmel, R., Smart, R.L. & Lattanzi, M.G. (2000) *Astron. Astrophys.* **354**, 67.
Drimmel, R. & Spergel, D.N. (2001) *Astrophys. J.* **556**, 181.
García-Ruiz, I., Kuijken, K. & Dubinski, J. (2002) *Mon. Not. R. Astron. Soc.* **337**, 459.
Kramer, M., Bell, J.F., Manchester, R.N., et al. (2003) *Mon. Not. R. Astron. Soc.* **342**, 1299.
López-Corredoira, M., Cabrera-Lavers, A., Garzón, F. & Hammersley, P.L. (2002a) *Astron. Astrophys.* **394**, 883.
López-Corredoira, M., Betancort-Rijo, J. & Beckman, J.E. (2002b) *Astron. Astrophys.* **386**, 169.
Lyne, A.G. , Manchester, R.N. & Taylor, J.H. (1985) *Mon. Not. R. Astron. Soc.* **213**, 613.
Manchester, R.N., et al. (2002) *ATNF Pulsar Catalogue*, http://www.atnf.csiro.au/research/pulsar/psrcat
Manchester, R.N., Lyne, A.G., Camilo, F., et al. (2001) *Mon. Not. R. Astron. Soc.* **328**, 17.
Morris, D.J., Hobbs, G., Lyne, A.G., et al. (2002) *Mon. Not. R. Astron. Soc.* **335**, 275.
Tsuchiya, T. (2002) *New Astron.* **7**, 293.